

Banner appropriate to article type will appear here in typeset article

Natural convection in a vertical channel. Part 3. Bifurcations of many (additional) unstable equilibria and periodic orbits

Zheng Zheng¹, Laurette S. Tuckerman²† and Tobias M. Schneider¹

¹Emergent Complexity in Physical Systems Laboratory (ECPS), École Polytechnique Fédérale de Lausanne, CH 1015 Lausanne, Switzerland

²Physique et Mécanique des Milieux Hétérogènes (PMMH), CNRS, ESPCI Paris, PSL University, Sorbonne Université, Université de Paris, 75005 Paris, France

(Received xx; revised xx; accepted xx)

Vertical thermal convection system exhibits weak turbulence and spatio-temporally chaotic behavior. In this system, we report seven equilibria and 26 periodic orbits, all new and linearly unstable. These orbits, together with four previously studied in [Zheng *et al.* \(2024c\)](#) bring the number of periodic orbit branches computed so far to 30, all solutions to the fully non-linear three-dimensional Navier-Stokes equations. These new invariant solutions capture intricate flow patterns including straight, oblique, wavy, skewed and distorted convection rolls, as well as bursts and defects in rolls. Most of the solution branches show rich spatial and/or spatio-temporal symmetries. The bifurcation-theoretic organisation of these solutions are discussed; the bifurcation scenarios include Hopf, pitchfork, saddle-node, period-doubling, period-halving, global homoclinic and heteroclinic bifurcations, as well as isolas. Given this large number of unstable orbits, our results may pave the way to quantitatively describing transitional fluid turbulence using periodic orbit theory.

Key words: thermal convection, nonlinear dynamical systems, bifurcation, symmetry

1. Introduction

The vertical thermal convection system is a classical and fundamental model in fluid dynamics, describing the motion of a fluid bounded by two vertical walls maintained at different temperatures. The fluid layer is driven by both buoyancy forces arising from horizontal temperature gradients and shear forces. Convection plays a crucial role in a wide range of natural and industrial processes, including atmospheric and oceanic circulation, mantle convection, and thermal management in engineering applications. Understanding the fundamentals of this system is essential for improving climate models, optimizing energy-efficient cooling systems, and enhancing mixing efficiency in physicochemical and industrial processes.

† Email address for correspondence: laurette.tuckerman@espci.fr

Like the well-known and well-studied Rayleigh-Bénard convection, vertical convection is also an ideal system for studying pattern formation above the onset of convection. Recent advances in experimental, numerical, and theoretical studies continue to refine our understanding of the stability, transition, turbulence, and heat transport mechanisms which are governed by the deterministic flow equations; these make vertical convection a subject of ongoing interest in fluid mechanics research. We refer readers to the introductions of the two previous papers in this series (Zheng *et al.* 2024b,c) for a more complete literature review of this field.

Using the methodology described in Zheng *et al.* (2024b,c), we consider the vertical convection system as a (very) high-dimensional non-linear dynamical system and employ the dynamical-systems-based approach to investigate the flow dynamics. This approach has been established as a paradigm to study transition to turbulence in various shear-dominated flows; see reviews in Kawahara *et al.* (2012); Graham & Floryan (2021) and references therein. Note that here, we use the word turbulence to refer to spatio-temporal chaos. In the infinite-dimensional phase space of the Navier-Stokes equations, turbulence is viewed as a chaotic walk through a forest of non-chaotic invariant solutions (particularly fixed points and periodic orbits). While equilibria may reproduce characteristic features of the flow, they are time-independent and so the information contained within such solutions is limited. However, unstable periodic orbits are much more dynamically important and are believed to be transiently visited by a weakly turbulent flow, and to form the skeleton and building blocks of the chaotic dynamics of transitional turbulence (Cvitanović 1991; Kawahara & Kida 2001).

In our vertical convection system, the control parameters are Rayleigh number (Ra) which is proportional to the temperature difference between the two walls and Prandtl number (Pr), which is the ratio between kinematic viscosity and thermal diffusivity. In addition to individual invariant solutions that are identified at fixed control parameters of the system, a bifurcation analysis via parametric continuations in one of the control parameters (Ra in this work) may reveal the bifurcation-theoretic origins of solutions and connections between them. A prominent example is in plane Couette flow; Reetz *et al.* (2019) constructed the first equilibrium solution underlying the self-organized oblique turbulent-laminar stripe pattern, and suggested that it emerges from the well-studied Nagata equilibrium (Nagata 1990). Many other examples in convective systems can be found in Borońska & Tuckerman (2010a,b), Reetz & Schneider (2020a); Reetz *et al.* (2020b) and Zheng *et al.* (2024b,c).

The present work follows two previous numerical investigations (Gao *et al.* 2018; Zheng *et al.* 2024c). Gao *et al.* (2018) have surveyed the flow regimes in a three-dimensional computational domain of size $[L_x, L_y, L_z] = [1, 8, 9]$, depicted in figure 1, by systematically increasing the Rayleigh number from the onset of convection at $Ra = 5707$ to $Ra \approx 6300$ (with $Pr = 0.71$ corresponding to air). Zheng *et al.* (2024c) used the same domain size, constructed invariant solutions, and extended the upper limit to $Ra \approx 6400$; a sequence of bifurcations was determined, and six equilibria and four time-periodic solutions were analyzed in detail. In addition to these known solutions, we present here 33 new unstable invariant solutions, including seven equilibria and 26 periodic orbits, and we have extended the Rayleigh number range to $Ra \approx 6650$. Even though the increase in Ra in each paper may seem insignificant and negligible compared to fully turbulent convection, the emerging complexity of the bifurcation problem is indeed already overwhelming.

The new solutions that we will discuss are mainly found by the standard recurrent flow analysis which uses time-dependent simulations to locate states at which nearly-periodic solutions or near recurrences is detected, and uses them as initial conditions for Newton solving. By construction, then, the new solutions are embedded in the trajectories followed by the flow. The new periodic orbits not only capture important dynamics of the transitional

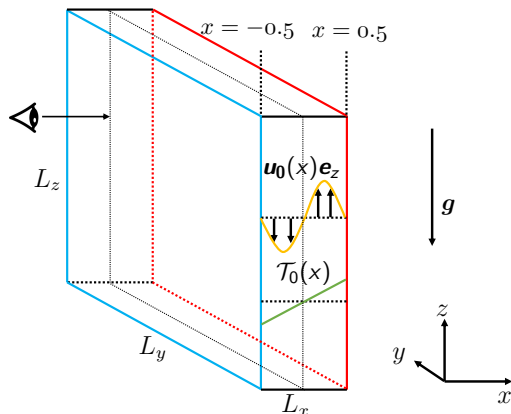


Figure 1: Vertical convection cell with size $[L_x, L_y, L_z] = [1, 8, 9]$. The flow is bounded between two fixed walls at $x = \pm 0.5$ at which the flow is heated and cooled respectively. We visualize the flow on the y - z plane at $x = 0$ (dotted), from left to right as indicated by the eye and arrow. The laminar velocity $\mathbf{u}_0(x) = \sqrt{Ra/Pr}(x/4 - x^3)/6 \mathbf{e}_z$ and temperature $\mathcal{T}_0(x) = x$ of this system are traced as an orange curve and a green line, respectively.

flow, but also give hope that they may act as a basis to predict the statistical quantities of the dynamics; see [Chandler & Kerswell \(2013\)](#); [Cvitanović \(2013\)](#); [Lucas & Kerswell \(2015\)](#); [Page et al. \(2024\)](#) for recent analysis of this point. In this work, we will focus on the bifurcation-theoretic origins, terminations, and connections between these solutions; our upcoming manuscript will explore the statistical description of the dynamics based on periodic orbits.

The rest of the manuscript is structured as follows. The numerical methods are summarized in §2. We discuss in §3 the new fixed points and in §4 the new periodic orbits, with a focus on their bifurcation scenarios. The manuscript will conclude with future research directions in §5.

2. System, computation of invariant solutions and symmetries

As the numerical methods used in the current research are exactly the same as those described in our precedent Part 1 and Part 2 papers, we refer readers to [Zheng et al. \(2024b,c\)](#) for detailed descriptions of the governing equations, laminar base solutions, boundary conditions, symmetries of the system, computation (including parametric continuation and linear stability analysis) of invariant solutions, as well as numerical visualizations. Here, we will succinctly summarize the key ingredients.

The Oberbeck–Boussinesq equations that govern our vertical convection system are

$$\frac{\partial \mathbf{u}}{\partial t} + (\mathbf{u} \cdot \nabla) \mathbf{u} = -\nabla p + \left(\frac{Pr}{Ra}\right)^{1/2} \nabla^2 \mathbf{u} + \mathcal{T} \mathbf{e}_z, \quad (2.1a)$$

$$\frac{\partial \mathcal{T}}{\partial t} + (\mathbf{u} \cdot \nabla) \mathcal{T} = \left(\frac{1}{Pr Ra}\right)^{1/2} \nabla^2 \mathcal{T}, \quad (2.1b)$$

$$\nabla \cdot \mathbf{u} = 0. \quad (2.1c)$$

Equations (2.1) with periodic boundary conditions (in y and z), Dirichlet boundary conditions (in x), and a zero mean pressure gradient (in y and z) integral constraint, are simulated numerically by using the Channelflow 2.0 code ([Gibson et al. 2019](#)). As in [Zheng et al.](#)

(2024c), we use a computational domain of size $[L_x, L_y, L_z] = [1, 8, 9]$ and discretize it by $[N_x, N_y, N_z] = [31, 96, 96]$ Chebychev-Fourier–Fourier modes, see figure 1. In addition to the grid resolution criterion discussed in §2.2 of Zheng *et al.* (2024b), we carried out a grid independence study by increasing $[N_x, N_y, N_z]$ to $[41, 136, 136]$ modes; the results are described in Appendix A.

The symmetries of the system are:

$$\pi_y[u, v, w, \mathcal{T}](x, y, z) \equiv [u, -v, w, \mathcal{T}](x, -y, z), \quad (2.2a)$$

$$\pi_{xz}[u, v, w, \mathcal{T}](x, y, z) \equiv [-u, v, -w, -\mathcal{T}](-x, y, -z), \quad (2.2b)$$

$$\tau(\Delta y, \Delta z)[u, v, w, \mathcal{T}](x, y, z) \equiv [u, v, w, \mathcal{T}](x, y + \Delta y, z + \Delta z), \quad (2.2c)$$

which generate the group $S \equiv \langle \pi_y, \pi_{xz}, \tau(\Delta y, \Delta z) \rangle \sim [O(2)]_y \times [O(2)]_{x,z}$. The laminar base flow has symmetry $[O(2)]_y \times [O(2)]_{x,z}$, but symmetries are often sequentially broken at each bifurcation. We will discuss the symmetries of each solution in §3 and §4. In addition, symmetries are also used as a tool to find invariant solutions in this work, because if solutions have such symmetries, they are usually less unstable in the constrained symmetry subspace, thus less difficult to find and converge.

Invariant solutions (fixed points and periodic orbits) are state vectors $\mathbf{x}^*(t)$ satisfying

$$\mathcal{G}(\mathbf{x}^*) = \sigma \mathcal{F}^T(\mathbf{x}^*) - \mathbf{x}^* = 0, \quad (2.3)$$

where σ is a symmetry operator and \mathcal{F}^T is the time-evolution operator integrating (2.1) from an initial state \mathbf{x}^* over a finite time period T . T is arbitrary for a steady solution, and is the period of a time-periodic solution. The periodic orbits that we will discuss in §4 are of three types. Periodic orbits (POs) are solutions which recur exactly after a period ($\sigma \equiv 1$ in (2.3)). Relative periodic orbits (RPOs) are orbits whose shortest recurrence occurs for a non-trivial symmetry operation, e.g. $\sigma \equiv \tau(\Delta y, \Delta z)$. Pre-periodic orbits (PPOs) are RPOs which recur exactly after some finite number of periods. (That is, PPOs are RPOs in which σ does not contain translations by irrational multiples of L_y or L_z .) In most of the later figures, we use T to denote periods for PO, relative periods for RPO, and pre-periods for PPO. Whenever we discuss a period T of an orbit in text, we specify to which type of period it refers; in most cases, it is the shortest period for which (2.3) holds for some σ .

Invariant solutions are computed by the shooting-based Newton method, with initial guesses generated by a systematic recurrent flow analysis. The success rate for converging to an invariant solution from one of these initial guesses is roughly 40%. These solutions are then parametrically continued in Rayleigh number to construct bifurcation diagrams. We define the temperature deviation $\theta \equiv \mathcal{T} - \mathcal{T}_0$ from the conductive state \mathcal{T}_0 shown in figure 1. We use its L_2 -norm $\|\theta\|_2$ to plot bifurcation diagrams throughout §3 and §4. The linear stability of converged states is evaluated by the Arnoldi algorithm. All of the 33 new solution branches are linearly unstable; they will be shown as solid curves in bifurcation diagrams. The flows (and eigenvectors) are visualized via their temperature fields θ on the y - z plane at $x = 0$, see figure 1. Note that for clarity we have intentionally omitted color bars in all snapshots while insuring that snapshots in one figure share the same color bar.

3. Unstable fixed points

In addition to the six equilibrium solutions (FP1–FP6) presented in Zheng *et al.* (2024c), we discuss here seven new unstable equilibria: FP7–FP13. These equilibria are relevant for the discussion on Hopf and global bifurcations of periodic orbits in §4. A bifurcation diagram including all of the new steady states as well as FP1, FP2 and FP4 (FP3, FP5 and FP6 are not plotted to avoid clutter) is illustrated in figure 2(a). All of the equilibria are continued forward

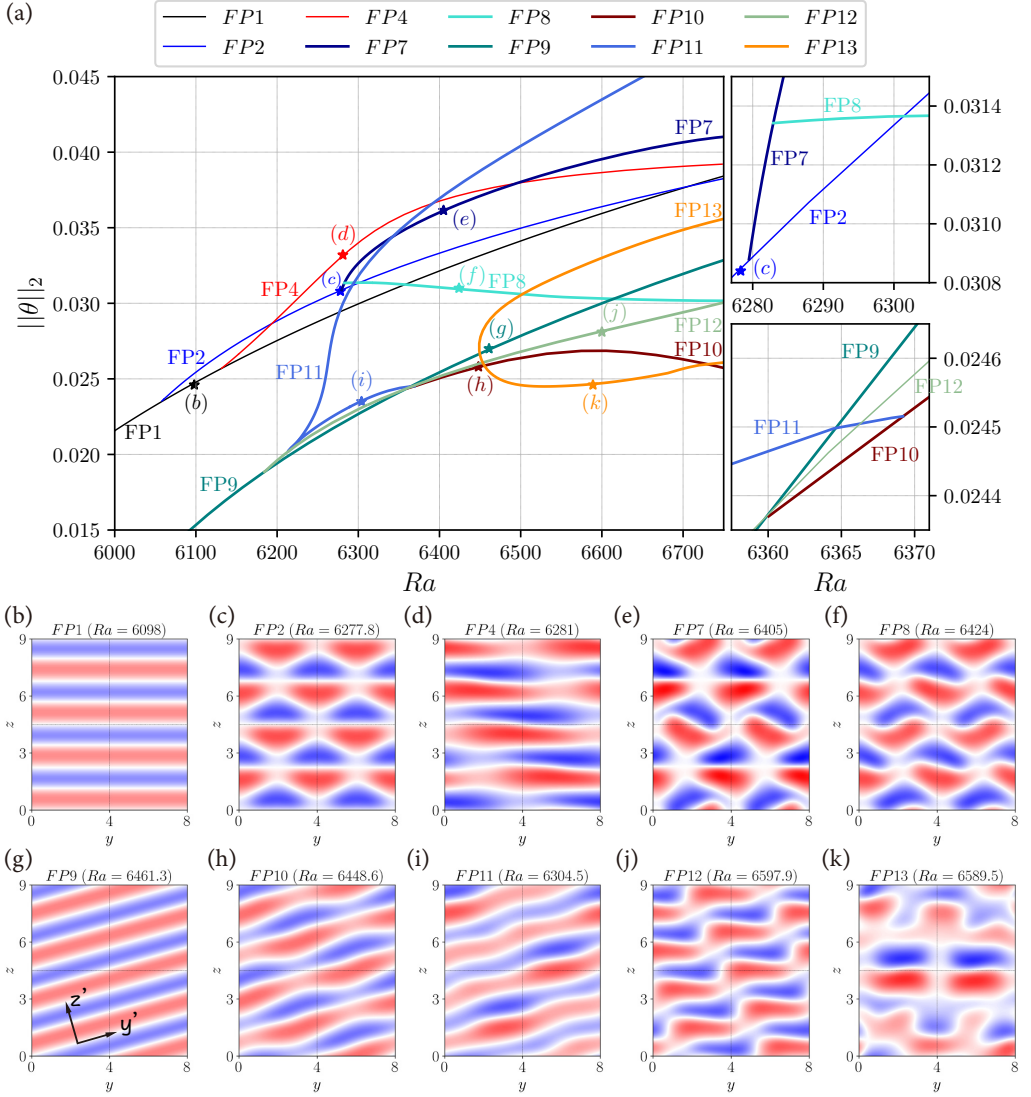


Figure 2: (a) Bifurcation diagram of fixed points and (b-k) flow structures visualized via the midplane temperature field. (b) FP1, (c) FP2 and (d) FP4 have been presented in [Zheng et al. \(2024c\)](#) and are shown with thinner curves in (a). All branches shown are unstable, with the exception of FP1 for $Ra < 6056$ and of FP2 for $6056 < Ra < 6058.5$. Two enlarged diagrams are shown on the right zooming in on the $FP2 \rightarrow FP7 \rightarrow FP8$ and $FP9 \rightarrow FP10 \rightarrow FP11$ bifurcations. (e) FP7 bifurcates from FP2 at $Ra = 6279.5$; (f) FP8 bifurcates from FP7 at $Ra = 6282.9$. (g) FP9 bifurcates from the unstable base state at $Ra = 5941$; (h) FP10 bifurcates from FP9 at $Ra = 6360$; (i) FP11 bifurcates from FP10 at $Ra = 6369.2$; (j) FP12 bifurcates from FP9 at $Ra = 6184$. (k) FP13 undergoes a saddle-node bifurcation at $Ra = 6449$ and both upper and lower branches exist at least until $Ra = 6800$.

in Rayleigh number until at least $Ra = 6750$. Note that many other branches of equilibria (and periodic orbits) exist, which we have not followed or shown on these diagrams.

3.1. FP7 and FP8

We begin our survey by briefly discussing FP1 and FP2. Equilibrium FP1 (2D rolls) is shown in figure 2(b) and contains four straight convection rolls of wavelength $\lambda_{FP1} = 9/4 = 2.25$

whose axes are oriented in the y direction. Equilibrium FP2 bifurcates from FP1 at $Ra = 6056$. FP2 is called wavy rolls in Gao *et al.* (2018) and diamond rolls in Zheng *et al.* (2024c), and is shown in figure 2(c). (The list of generators for FP2 in (3.1) omits $\tau(0, L_z/2)$, contained in (3.1) of Zheng *et al.* (2024c), because it can be produced by the other generators and is hence redundant.) Equilibrium FP7, shown in figure 2(e), bifurcates from FP2 at $Ra = 6279.5$ in a supercritical pitchfork bifurcation, in which the π_y reflection and four-fold translation (along both diagonals) symmetries are broken. Equilibrium FP8, shown in figure 2(f), bifurcates from FP7 in a supercritical pitchfork bifurcation at $Ra = 6282.9$, in which the $\pi_y\tau(0, L_z/2)$ symmetry is broken. FP8 gives rise to PO23 and PO24 in two Hopf bifurcations, see §4.7. The symmetry groups of FP1, FP2, FP7 and FP8 are

$$\begin{aligned}
 \text{FP1: } & \langle \pi_y, \tau(\Delta y, 0), \pi_{xz}, \tau(0, L_z/4) \rangle && \sim [O(2)]_y \times [D_4]_{xz}; \\
 \text{FP2: } & \langle \tau(L_y/2, 0), \pi_{xz}, \pi_y, \tau(L_y/4, -L_z/4) \rangle && \sim D_2 \times D_4; \\
 \text{FP7: } & \langle \tau(L_y/2, 0), \pi_y\pi_{xz}, \pi_y\tau(0, L_z/2) \rangle && \sim D_2 \times Z_2; \\
 \text{FP8: } & \langle \tau(L_y/2, 0), \pi_y\pi_{xz} \rangle && \sim D_2.
 \end{aligned} \tag{3.1}$$

3.2. FP9-FP12

Equilibrium FP9, shown in figure 2(g), bifurcates from the homogeneous unstable base flow at $Ra = 5941$ (not shown in figure 2a) in a supercritical pitchfork bifurcation. FP9 has four pairs of oblique but straight convection rolls of wavelength $\lambda_{\text{FP9}} = 2L_z/\sqrt{L_z^2/16 + L_y^2} \approx 2.166$ each, in the direction perpendicular to the rolls. The oblique angle with respect to the y -direction is $\gamma = \arctan(0.25L_z/L_y) \approx 15.7^\circ$. Because FP9-FP12 all share this oblique orientation, we introduce tilted coordinates

$$\begin{pmatrix} y' \\ z' \end{pmatrix} = \begin{pmatrix} \cos \gamma & \sin \gamma \\ -\sin \gamma & \cos \gamma \end{pmatrix} \begin{pmatrix} y \\ z \end{pmatrix}, \tag{3.2}$$

which are drawn in figure 2(g). In the tilted coordinates, we consider a virtual computational domain having length $L'_z = 4\lambda_{\text{FP9}} \approx 8.664$ in z' and $L'_y \approx 15$ in y' . (The length $L'_y \approx 15$ is three times the wavelength corresponding to the prominent structure along y' in FP10 and FP11, and four times the wavelength corresponding to the wavy structure in FP12. Introducing this length will be convenient for the description of symmetry groups.) In this tilted domain, FP9 has $O(2)$ symmetry in y' and D_4 symmetry in xz' ; see (3.3).

Equilibrium FP10, shown in figure 2(h), bifurcates from FP9 at $Ra = 6360$ in a supercritical pitchfork bifurcation. In this bifurcation, the $O(2)$ symmetry of FP9 along y' is broken and succeeded by a discrete (two-fold) translation. In z' , the four-fold translation must now be combined with a discrete (four-fold) translation in y' in order to remain a symmetry of the flow. Finally, the two independent reflection symmetries are replaced by a single combined reflection $\pi_{y'}\pi_{xz'}$.

Equilibrium FP11, shown in figure 2(i), bifurcates from FP10 at $Ra = 6369.2$ in a subcritical pitchfork bifurcation. FP11 then undergoes a saddle-node bifurcation at $Ra = 6213.5$ and continues to exist at least until $Ra = 7000$. In going from FP10 to FP11, the spatial periodicity along y' changes from $L'_y/2$ to L'_y , while other symmetries are retained. FP11 gives rise to PO14 in a Hopf bifurcation, see §4.5.1 in which FP9 (and FP12 below) will also be relevant.

Equilibrium FP12, shown in figure 2(j), also bifurcates from FP9, in a supercritical pitchfork bifurcation at $Ra = 6184$. In y' , the $O(2)$ symmetry of FP9 is succeeded by a four-fold translation, the four-fold translation in z' is retained, and the two reflection symmetries are replaced by the single combined reflection $\pi_{y'}\pi_{xz'}$.

The symmetry groups of FP9-FP12 are

$$\begin{aligned}
 \text{FP9: } & \langle \pi_{y'}, \tau(\Delta y', 0), \pi_{xz'}, \tau(0, L'_z/4) \rangle & \sim [O(2)]_{y'} \times [D_4]_{xz'}; \\
 \text{FP10: } & \langle \pi_{y'} \pi_{xz'}, \tau(L'_y/2, 0), \tau(L'_y/4, L'_z/4) \rangle & \sim [D_2]_{y'} \times [Z_4]_{xz'}; \\
 \text{FP11: } & \langle \pi_{y'} \pi_{xz'}, \tau(L'_y/4, L'_z/4) \rangle & \sim [Z_2]_{y'} \times [Z_4]_{xz'}; \\
 \text{FP12: } & \langle \pi_{y'} \pi_{xz'}, \tau(L'_y/4, 0), \tau(0, L'_z/4) \rangle & \sim [D_4]_{y'} \times [Z_4]_{xz'};
 \end{aligned} \tag{3.3}$$

3.3. FP13

FP13 is shown in figure 2(k) and exists beyond $Ra = 6800$, where we stopped the continuation; its bifurcation-theoretic origin remains unclear. In the Rayleigh number range that we consider, FP13 undergoes one saddle-node bifurcation at $Ra = 6449$. Its symmetry group is

$$\text{FP13: } \langle \pi_y \pi_{xz} \rangle \sim Z_2. \tag{3.4}$$

4. Unstable periodic orbits

In this section we discuss 26 newly identified unstable periodic orbits RPO5-PPO30. The bifurcation diagram shown in figure 3 includes PO2-PPO30 (PO1-PO4 are discussed in Zheng *et al.* (2024c)) to give an overview of the bifurcation scenarios. Separated bifurcation diagrams for smaller groups of periodic orbits will be shown in figures 4, 5, 7, 8, 11, 15 and 20. Given the complexity of all of the bifurcation diagrams, we recommend reading each diagram by first focusing on the plot of the temporal period and then comparing it with that of the temperature norm. The reason is that the quantity $\|\theta\|_2$ might sometimes be close for multiple orbits and for one orbit along the branch (due to saddle-node bifurcations), but the periods of the orbits are more distinct and thus lead to a better understanding of the bifurcation scenarios. Note that the naming for these orbits (POX) is based purely on the sequential order in which they have been found. In this work, we focus on Rayleigh numbers up to $Ra \approx 6650$, thus $\sim 16.5\%$ above the onset of convection, even though some orbits can be continued to much higher Rayleigh numbers. We do not discuss if and how their branches end there.

The bifurcation scenarios explored include Hopf, pitchfork, saddle-node, period-doubling, period-halving, global homoclinic/heteroclinic bifurcations and isolas. Given the large number of orbits that we will discuss, this section is organized in terms of the symmetries of the orbits. The eight subsections below will discuss orbits identified in the following symmetry subspaces: four-fold translation along the domain diagonal with a non-commuting reflection: $\langle \pi_y \pi_{xz}, \tau(L_y/4, L_z/4) \rangle$ in §4.1; two-fold translation with a commuting reflection: $\langle \pi_y \pi_{xz}, \tau(L_y/2, L_z/2) \rangle$ in §4.2; four-fold translation: $\langle \tau(L_y/4, L_z/4) \rangle$ in §4.3; two-fold translation: $\langle \tau(L_y/2, L_z/2) \rangle$ in §4.4; three-fold translation with a non-commuting reflection: $\langle \pi_y \pi_{xz}, \tau(L_y/3, L_z/3) \rangle$ in §4.5; five-fold translation with a non-commuting reflection: $\langle \pi_y \pi_{xz}, \tau(L_y/5, L_z/5) \rangle$ in §4.6; and single reflection: $\langle \pi_y \pi_{xz} \rangle$ in §4.7. Orbits without any spatial symmetry will be presented in §4.8.

4.1. Symmetry subspace: reflection with four-fold translation

Seven orbits identified in the symmetry subspace $\langle \pi_y \pi_{xz}, \tau(L_y/4, L_z/4) \rangle \sim D_4$ will be discussed in this subsection. Due to this imposed symmetry constraint, the dynamics of these seven orbits all have a diagonal orientation and consist of diagonal excursions from more aligned states. We only show snapshots of RPO18 (figure 6) for illustration.

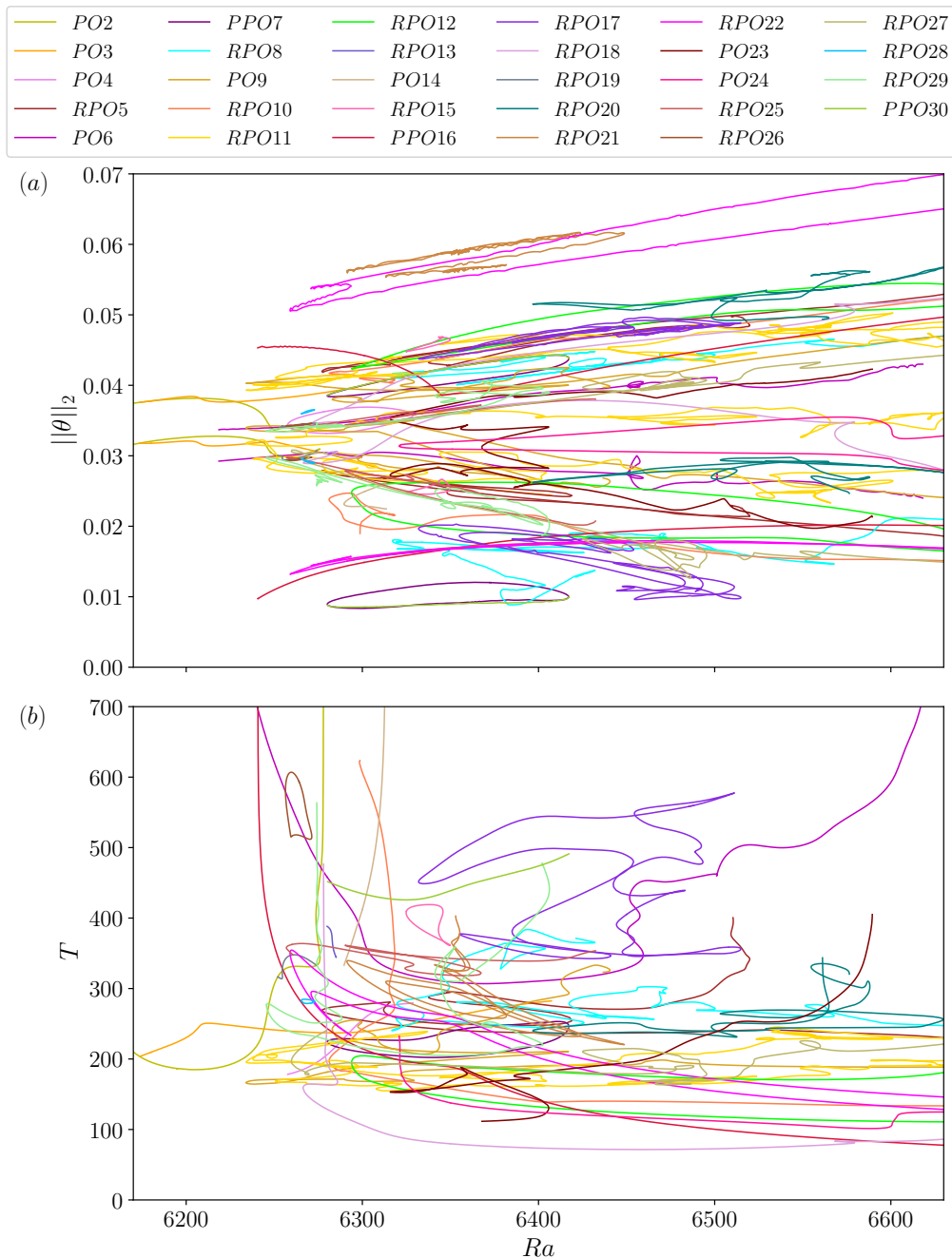


Figure 3: Temperature norms (a) and periods (b) of periodic orbits. PO, RPO and PPO stand for periodic orbit, relative periodic orbit and pre-periodic orbit, respectively. PO2-PO4 are discussed in detail in [Zheng et al. \(2024c\)](#). In (a), for each orbit, we show two curves, the maximum and minimum of $\|\theta\|_2$ along an orbit. All of RPO5-PPO30 are linearly unstable. The upper limit of (b) is set to $T = 700$, even though some orbits are continued to higher period. The bifurcation scenarios include Hopf, pitchfork, saddle-node, period-doubling, period-halving, global homoclinic/heteroclinic bifurcations and isolas. For more clarity, bifurcation diagrams for selected sets of orbits will be shown in figures [4](#), [5](#), [7](#), [8](#), [11](#), [15](#) and [20](#).

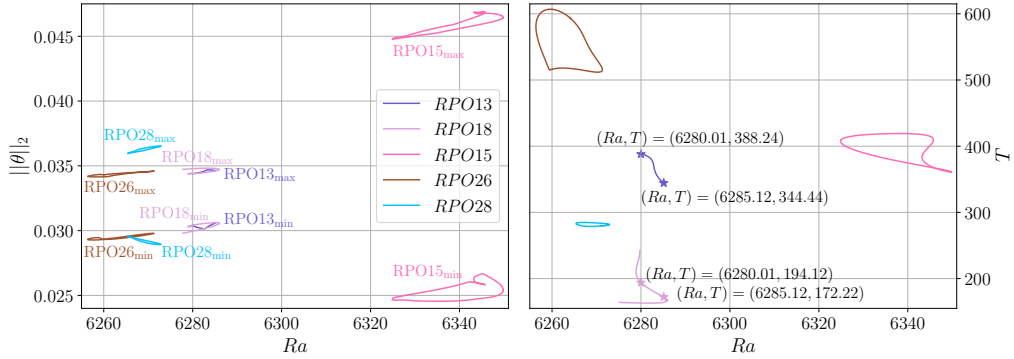


Figure 4: Temperature norms (left) and periods (right) of RPO13, RPO15, RPO26 and RPO28. Branch RPO13 bifurcates from and terminates on RPO18 (which is shown more completely in figure 5) in two period-doubling bifurcations. The bifurcation points are indicated by stars on the right plot. RPO15, RPO26 and RPO28 begin and terminate at saddle-node bifurcations and form isolas.

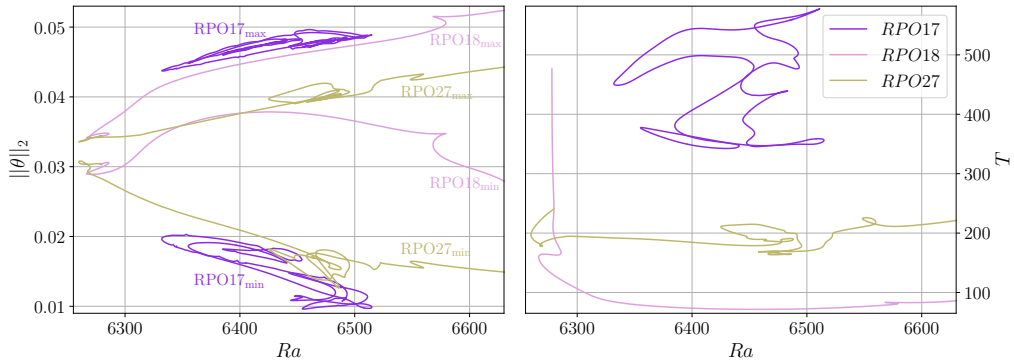


Figure 5: Temperature norms (left) and periods (right) of RPO17, RPO18 and RPO27. The RPO17 branch forms an isola. RPO18 bifurcates from FP2 in a global homoclinic bifurcation at $Ra = 6277.96$ and continues to exist up to at least $Ra = 6686$. RPO27 is generated from RPO18 in a pitchfork bifurcation at $Ra = 6279.7$ and continues to exist up to at least $Ra = 6650$.

4.1.1. RPO13: period-doubling bifurcations

RPO13 is found at $Ra = 6285$. Forward and backward continuation in Rayleigh number reveal that RPO13 bifurcates from and ends at RPO18 in two period-doubling bifurcations, at $Ra = 6280.01$ and 6285.12 , as indicated by the stars in figure 4. (RPO18 will be discussed in §4.1.3.)

4.1.2. RPO15, RPO17, RPO26 and RPO28: saddle-node bifurcations and isolas

We identify four isolas in this symmetry subspace. As the name implies, they do not bifurcate from any other states but only undergo several saddle-node bifurcations to turn back in Ra , as evidenced by figure 4 for RPO15, RPO26, RPO28, and by figure 5 for RPO17. One more isola with slightly different symmetry will be discussed in §4.2.2.

4.1.3. RPO18: saddle-node and global bifurcations

We found RPO18 at $Ra = 6350$ and continued it forwards up to $Ra = 6686$. Continuing backwards, RPO18 undergoes several saddle-node bifurcations and finally terminates in a global bifurcation by meeting FP2. The dynamics of RPO18 at $Ra = 6277.958$, the lowest

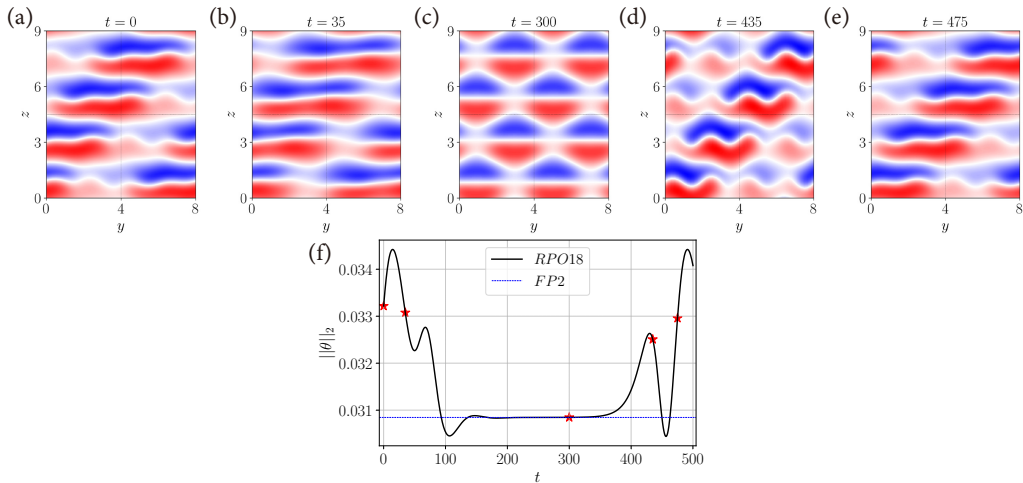


Figure 6: Dynamics of RPO18 at $Ra = 6277.958$ (close to the global bifurcation point) with relative period $T = 476.31$. (a-e) Snapshots of the midplane temperature field. (f) Time series from DNS. The five red stars indicate the moments at which the snapshots (a)-(e) are taken.

Rayleigh number that we have reached, is shown in figures 6(a-e). RPO18 resembles PO2, as presented in Zheng *et al.* (2024c): it has a clear oblique orientation. The global bifurcation is evidenced by the plateau in the time series in figure 6(f) and the divergence of its period in figure 5.

We have determined the eigenvector along which RPO18 approaches and escapes from FP2 by computing the leading eigenvalues of FP2 at $Ra = 6277.958$ within the symmetry subspace $\langle \pi_y \pi_{xz}, \tau(L_y/4, L_z/4) \rangle$, as was done in Zheng *et al.* (2024c). We find that RPO18 escapes from FP2 along eigendirection e_1 associated with eigenvalue $\lambda_1 = 0.031285$ and approaches FP2 via eigendirection e_2 associated with eigenvalue $\lambda_2 = -0.0138$. These eigenvectors turn out to be the same or symmetrically-related versions of those which are responsible for PO2 to escape from and to approach FP2. We do not show these to avoid repetition and refer readers to figures 9 and 10 of Zheng *et al.* (2024c) for details. Interestingly, the global bifurcations of PO2 and RPO18 occur at almost the same Rayleigh number, and we will see in §4.2.1 and §4.2.6 that FP2 gives rise to other global heteroclinic and homoclinic bifurcations.

4.1.4. RPO19: period-doubling and saddle-node bifurcations

As shown in figure 7, RPO19 bifurcates from and terminates on PO2 in two period-doubling bifurcations. As discussed in §4.2 of Zheng *et al.* (2024c), PO2 has a spatio-temporal symmetry and contains two pre-periodic orbits, each of half period of PO2. The periods of PO2 that we show in figure 7 (and figure 3b) correspond to full periods or twice the pre-periods. RPO19 also undergoes two saddle-node bifurcations at $Ra \approx 6254.6$, which are difficult to see in the figure.

4.2. Symmetry subspace: reflection with two-fold translation

Seven orbits identified in the symmetry subspace $\langle \pi_y \pi_{xz}, \tau(L_y/2, L_z/2) \rangle \sim D_2$ will be discussed in this subsection. Similarly to §4.1, this imposed symmetry leads the dynamics of most of the orbits to acquire a diagonal orientation. We will show snapshots of PO6 (diagonal), PPO7 (non-diagonal) and RPO10 (diagonal), for illustration.

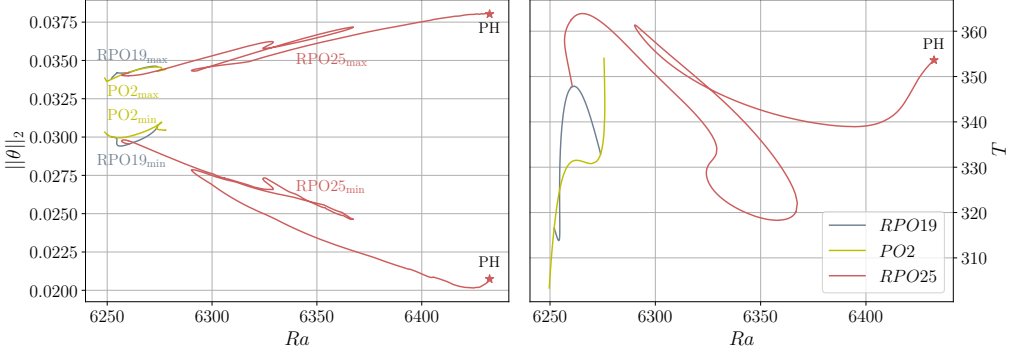


Figure 7: Temperature norms (left) and periods (right) of PO2, RPO19 and RPO25. Branch RPO19 bifurcates from and ends on PO2 (discussed in Zheng *et al.* (2024c)) at $Ra = 6252$ and $Ra = 6274$ in two period-doubling bifurcations. RPO25 bifurcates from RPO19 at $Ra = 6260.5$ in a pitchfork bifurcation, undergoes saddle-node bifurcations, and terminates in a period-halving bifurcation (marked by PH) on another branch that is not shown or studied in this paper.

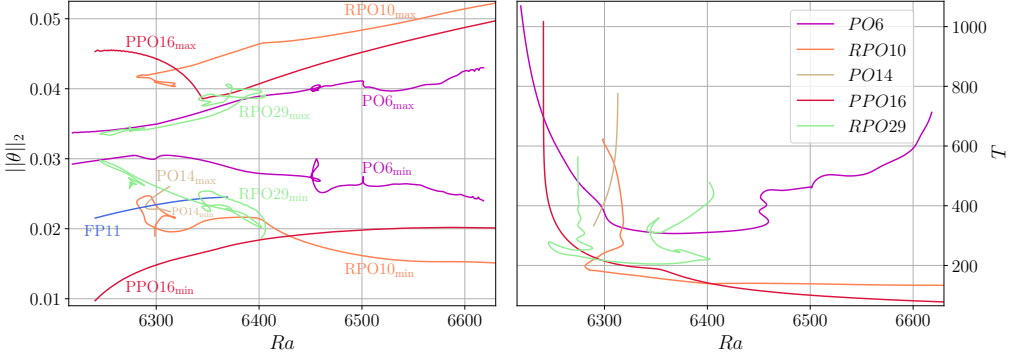


Figure 8: Temperature norms (left) and periods (right) of PO6, RPO10, PO14, PPO16 and RPO29. Branch PO6 approaches a heteroclinic cycle linking two symmetrically-related versions of FP2 in a global bifurcation at $Ra \approx 6218.6$, at which its period diverges. At higher Rayleigh numbers, PO6 undergoes saddle-node bifurcations and continues to exist at least until $Ra = 6615$. RPO10 possibly bifurcates from FP4 in a global bifurcation at $Ra \approx 6298.7$ and continues to exist at least until $Ra = 6650$. PO14 bifurcates from FP11 in a Hopf bifurcation and terminates in a global bifurcation by meeting FP9. PPO16 is created from FP9 in a global bifurcation at $Ra \approx 6240.6$ and continues to exist until at least $Ra = 6656.5$. RPO29 bifurcates from FP4 at $Ra \approx 6274.14$ and terminates on FP2 at $Ra \approx 6402$ in two global bifurcations.

4.2.1. PO6: saddle-node and global bifurcations

We first observed PO6 at $Ra = 6280$. PO6 has the spatio-temporal symmetry

$$(u, v, w, \theta)(x, y, z, t + T/2) = \pi_y(u, v, w, \theta)(x, y + L_y/2, z, t). \quad (4.1)$$

Like PO2, discussed in Zheng *et al.* (2024c), PO6 can be understood as a pre-periodic orbit with a total period (shown in figures 3(b) and 8) that is twice its pre-period. Continuing PO6 backwards, it approaches a heteroclinic cycle linking two symmetrically-related versions of FP2. From $Ra = 6280$ to $Ra = 6218.6$, the period of PO6 increases monotonically to $T = 1069.1$. (We have omitted the range $700 < T < 1069.1$ in figure 3(b) to better show the periods of other orbits.) At the global bifurcation point at slightly lower Rayleigh number, the period should diverge. Compare with, for example, the slope of PO2, PO14, PPO16,

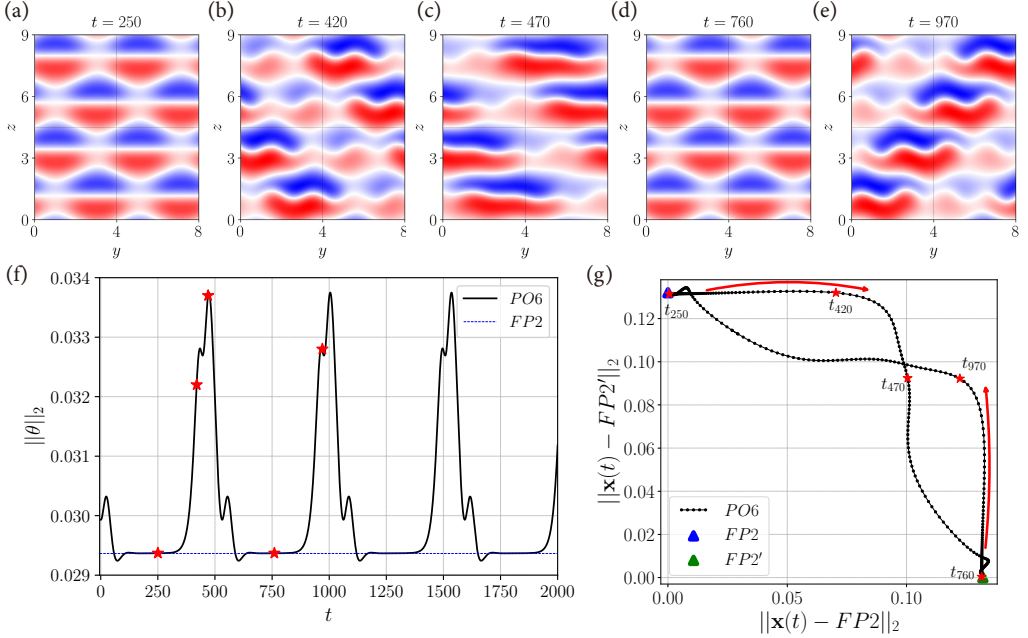


Figure 9: (a-e) Snapshots of the dynamics of PO6 at $Ra = 6218.6$. Snapshots (a) and (d) show states which are close to two symmetry-related versions of FP2. (f) Time series of PO6 at $Ra = 6218.6$ (with period $T = 1069.1$). (g) Phase space projection at $Ra = 6218.6$ close to the global bifurcation point. The curve shows PO6 and triangles show two symmetry-related FP2 states involved in the heteroclinic cycle. In (f) and (g), the five red stars indicate the moments at which the snapshots (a)-(e) are taken. In (g), the red arrows show the direction of the trajectory.

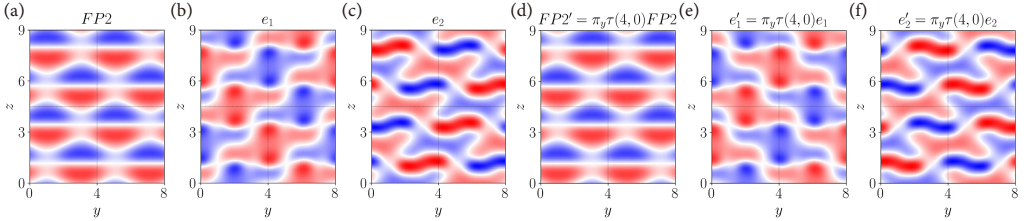


Figure 10: At $Ra = 6218.6$, (a) FP2, (b) its unstable eigenmode e_1 and (c) its stable eigenmode e_2 . (d) $FP2' \equiv \pi_y \tau(4, 0) FP2$, (e) its unstable eigenmode $e_1' \equiv \pi_y \tau(4, 0) e_1$, and (f) its stable eigenmode $e_2' \equiv \pi_y \tau(4, 0) e_2$. The wavenumbers of the equilibria and eigenmodes in the y direction suggest a 1:2 mode interaction.

RPO18 and RPO29. We have been unable to continue PO6 further due to limits on numerical precision.

The dynamics of PO6 at $Ra = 6218.6$, close to the global bifurcation point, is shown in figures 9(a-e). PO6 resembles PO2 presented in Zheng *et al.* (2024c) and RPO18 above. The dynamics of each half period of PO6 has four-fold translation symmetry along one of the diagonals, either $\langle \tau(L_y/4, L_z/4) \rangle$ or $\langle \tau(L_y/4, -L_z/4) \rangle$; compare figures 9(b) and 9(e). The only symmetry possessed instantaneously by all members of PO6 is $\langle \tau(L_y/2, L_z/2) \rangle$. The heteroclinic bifurcation is evidenced by the plateaus in the time series in figure 9(f) as well as by the phase space projection in figure 9(g). The eigenvectors along which PO6 approaches and escapes from FP2 (and $FP2' \equiv \pi_y \tau(L_y/2, 0) FP2$) are shown in figure 10, together with the phase of FP2 (and $FP2'$).

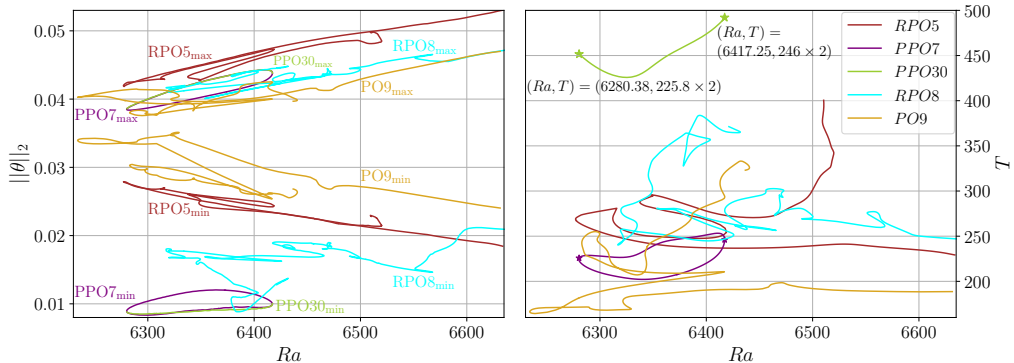


Figure 11: Temperature norms (left) and periods (right) of RPO5, PPO7, RPO8, PO9 and PPO30. Branches RPO5, RPO8 and PO9 undergo saddle-node bifurcations and are continued until $Ra = 6635$ for one of their endpoints. At the other endpoints, RPO5 possibly bifurcates from FP4 in a global bifurcation, and the termination of RPO8 and PO9 are unclear. PPO7 undergoes saddle-node bifurcations and forms an isola. PPO30 bifurcates from and terminates on PPO7 in two period-doubling bifurcations.

To show that PO6 approaches a robust heteroclinic cycle as is the case for PO2, we identify two subspaces within the symmetry space of FP2:

$$\begin{aligned} S &\equiv \text{Fix}|\langle \pi_y, \pi_{xz}, \tau(L_y/4, -L_z/4) \rangle, \\ S' &\equiv \text{Fix}|\langle \pi_y, \pi_{xz}, \tau(L_y/4, L_z/4) \rangle. \end{aligned} \quad (4.2)$$

For the flow restricted to subspace S (S'), FP2 is a saddle (sink), FP2' is a sink (saddle), and there exists a saddle-sink connection $\text{FP2} \rightarrow \text{FP2}'$ ($\text{FP2}' \rightarrow \text{FP2}$). More details of the conditions required for a robust heteroclinic cycle can be found in Krupa (1997); Reetz & Schneider (2020a) and §4.2.3 of Zheng *et al.* (2024c). Like PO2, this robust cycle results from a 1:2 mode interaction (Armbruster *et al.* 1988).

We have continued PO6 forward in Rayleigh number up to $Ra = 6618.12$ where it has period $T = 712.76$. Along the branch, PO6 undergoes a sequence of saddle-node bifurcations between $6450 \lesssim Ra \lesssim 6460$ and then at $Ra \approx 6505$, as shown in figure 8. Beyond $Ra = 6550$, the period of PO6 increases monotonically and seems to diverge. Integrating PO6 at $Ra = 6618.12$ forward in time, we observe that its trajectory tends to visit two symmetrically-related FP2, with the time spent near FP2 substantially shorter than at $Ra = 6218.6$. We suggest that PO6 may bifurcate again from FP2 in another heteroclinic bifurcation slightly beyond $Ra = 6618.12$. However, since the continuation becomes computationally difficult for higher Rayleigh numbers, we have not been able to confirm this. We do not show snapshots of PO6 at $Ra = 6618.12$, as they do not differ substantially from those in figures 9(a-e).

4.2.2. PPO7: saddle-node bifurcations and isola

Like RPO15, RPO17, RPO26 and RPO28 that are discussed in §4.1.2, branch PPO7 also forms an isola, with two saddle-node bifurcations at $Ra = 6280.5$ and 6417.2 , as shown in figure 11. PPO7 gives rise to PPO30 via two period-doubling bifurcations that will be discussed later in §4.2.7.

The dynamics of PPO7 at $Ra = 6280.38$ (the period-doubling bifurcation point) is shown in figures 12(a-j). The simulation starts from a state close to the mustache rolls (FP5 in Zheng *et al.* (2024c)); the roll at the domain center (as well as corners due to $\tau(L_y/2, L_z/2)$ symmetry) then becomes more intense, distorted and ramified (figures 12b-e). At $t = 115$, the central roll pinches off and merges with neighboring rolls at $t = 130$. After a smooth

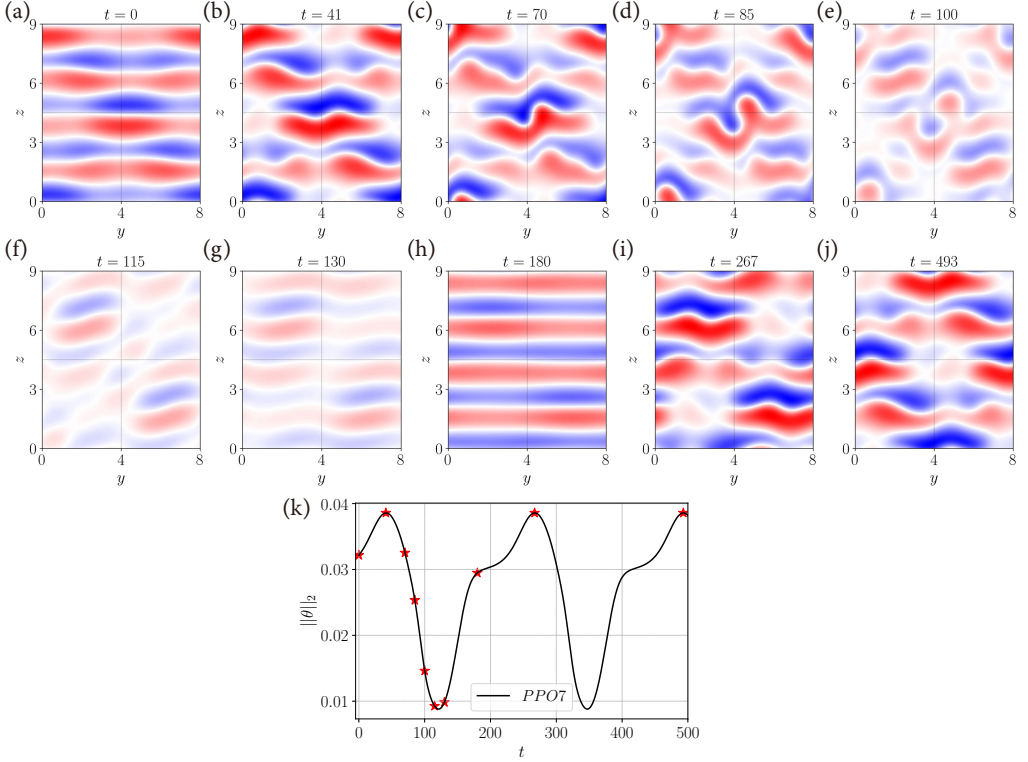


Figure 12: Dynamics of PPO7 at $Ra = 6280.38$ with pre-period $T = 226$. (a-j) Snapshots of the midplane temperature field. (k) Time series from DNS. The ten red stars indicate the moments at which the snapshots (a)-(j) are taken.

transition towards nearly straight rolls at $t = 180$, the trajectory returns to the distorted-roll state at $t = 267$.

PPO7 has the spatio-temporal symmetry:

$$(u, v, w, \theta)(x, y, z, t + T) = \pi_y(u, v, w, \theta)(x, y + L_y/4, z - L_z/4, t), \quad (4.3)$$

where $T = 226$ is the pre-period of PPO7 at $Ra = 6280.38$. After a pre-period, the state at $t = 267$, figure 12(i) is a reflected and translated version of the state at $t = 41$, figure 12(b); after integrating over a second pre-period, the states at $t = 493$ and $t = 41$ are related by $\sigma \equiv \tau(\pm L_y/2, 0)$ or $\tau(0, \pm L_z/2)$. Finally, after integrating during four pre-periods, the initial state matches the final state, i.e. PPO7 is a periodic orbit.

A remarkable feature of PPO7 in figure 3(a) is that its minimum temperature norm along the branch ($\|\theta\|_2 \approx 0.01$) is almost the lowest among all orbits. The faint figures 12(f-g) correspond to the moments of lowest temperature norm. These are the moments of cutting-joining-like dynamics of convection rolls, very similar to the longitudinal burst pattern observed by Daniels *et al.* (2000) experimentally and by Reetz *et al.* (2020b) numerically, at slightly different control parameters. The cutting-joining dynamics induces defects, disordered structures in rolls and roll-bursting; these contribute to the transition to turbulence. To the best of our knowledge, PPO7 may be the first (pre-)periodic orbit that captures these aspects of the dynamics.

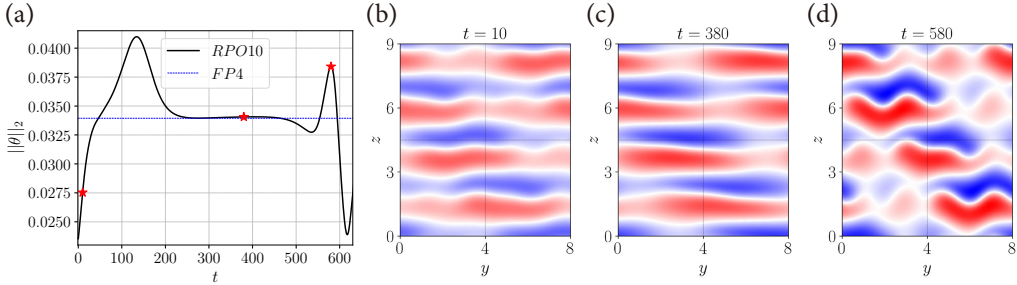


Figure 13: Dynamics of RPO10 at $Ra = 6298.686$ with relative period $T = 623.35$. (a) Time series of RPO10; the three red stars indicate the moments at which the snapshots (b)-(d) of the midplane temperature field are taken.

4.2.3. RPO10: saddle-node and global bifurcations

We first found RPO10 at $Ra = 6400$. Forward continuation in Ra shows that it exists until at least $Ra = 6675$ where we stopped the continuation. Continuing RPO10 backwards in Ra , it undergoes a sequence of saddle-node bifurcations after which its period increases monotonically, as evidenced by figure 8. We have been able to continue RPO10 until $Ra = 6298.686$ with relative period $T = 623.35$, shortly after the last saddle-node bifurcation at $(Ra, T) = (6298.39, 622.97)$.

Integrating RPO10 at $Ra = 6298.686$ in time, we observe a long plateau ($250 < t < 460$) in the time series shown in figure 13(a). The dynamics of RPO10 at this Ra is shown in figures 13(b-d). The states corresponding to the location of the plateau are very similar to FP4, in terms of both flow structure and temperature norm. This suggests that RPO10 disappears in a global homoclinic bifurcation by meeting FP4, although the slope of the last computed portion of $T(Ra)$ in figure 8 is not as close to vertical as the corresponding slopes for PO6, PO14, PPO16 and RPO29.

4.2.4. RPO25: pitchfork, saddle-node and period-halving bifurcations

As shown in figure 7, RPO25 bifurcates from RPO19 at $Ra = 6260.5$ in a pitchfork bifurcation, in which the translation symmetry $\tau(L_y/4, L_z/4)$ is broken to $\tau(L_y/2, L_z/2)$ and the reflection symmetry $\pi_y \pi_{xz}$ is retained. RPO25 then undergoes several saddle-node bifurcations and finally terminates in a period-halving bifurcation at $Ra = 6432.34$ (indicated in figure 7). We do not show or discuss the period-halved orbit in this work.

4.2.5. RPO27: pitchfork and saddle-node bifurcations

As shown in figure 5, RPO27 bifurcates from RPO18 at $Ra = 6279.7$ in a pitchfork bifurcation at which $\tau(L_y/4, L_z/4)$ symmetry is broken to $\tau(L_y/2, L_z/2)$ (with $\pi_y \pi_{xz}$ retained). It undergoes a sequence of saddle-node bifurcations, particularly between $Ra = 6420$ and 6500 , and we have continued it until $Ra = 6650$.

4.2.6. RPO29: saddle-node and global bifurcations

We first observed RPO29 at $Ra = 6300$. Its bifurcation diagram is shown in figure 8; we show its period again in figure 14(a). Backward continuation reveals the interesting feature of at least 13 saddle-node bifurcations (see figure 14(a) and probably even more if it could be continued further towards higher periods) before the global bifurcation. This observation is reminiscent of the homoclinic snaking of spatially localized solutions observed in various dynamical systems. In our case, we have checked that the states along the RPO29 branch do not show an increasing number of rolls or structures, nor an increasing number of peaks

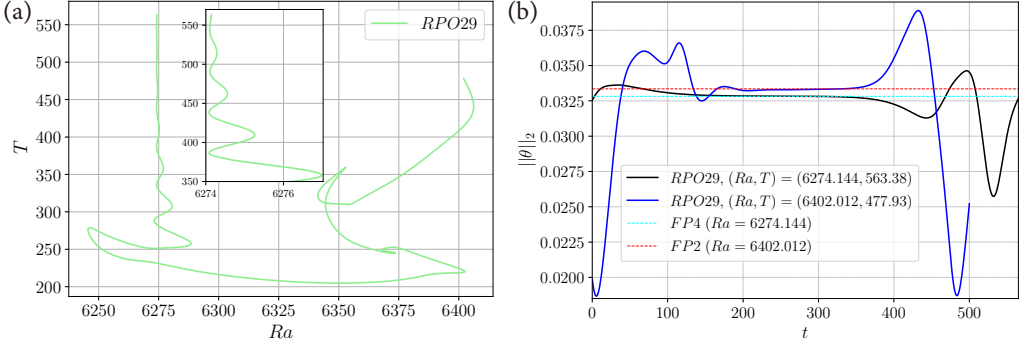


Figure 14: (a) Periods and (b) time series of RPO29. (Branch RPO29 also appears as part of figure 8.) The inset in (a) shows a sequence of saddle-node bifurcations before the global bifurcation at $Ra \approx 6274.14$. (b) Time series from the last continuation point (longest period) at $Ra = 6274.144$ and $Ra = 6402.012$. RPO29 approaches FP2 and FP4 in two different global homoclinic bifurcations at its two endpoints.

in a temporal sequence after each saddle-node bifurcation. We have no explanation for these successive saddle-node bifurcations. We have been able to continue RPO29 down to $Ra = 6274.144$, where it has relative period $T = 563.38$. Beyond this, there is a global bifurcation at which the period diverges. RPO29 undergoes successive approaches to FP4 (see time series in figure 14b), as is the case for RPO10 in §4.2.3; their behavior is also similar so we do not show snapshots for this orbit.

Continuing RPO29 forward from $Ra = 6300$, many saddle-node bifurcations are also seen and the branch also terminates in a global homoclinic bifurcation, this time by meeting FP2. We have been able to continue RPO29 until $(Ra, T) = (6402.012, 477.93)$. Even though we believe that this is still far from the actual global bifurcation point as the period is not yet very long, a close approach to FP2 is evidenced by a clear plateau (whose corresponding norm is very close to that of FP2) in the time series in figure 14(b) and by inspection of flow fields (not shown).

4.2.7. PPO30: period-doubling bifurcations

PPO30 bifurcates from and terminates on PPO7 in two period-doubling bifurcations, at $Ra = 6280.38$ and 6417.25 , indicated in figure 11. For PPO30,

$$\begin{aligned} (u, v, w, \theta)(x, y, z, t + T) &= (u, v, w, \theta)(x, y \pm L_y/2, z, t), \\ &= (u, v, w, \theta)(x, y, z \pm L_z/2, t), \end{aligned} \quad (4.4)$$

where T is the pre-period of PPO7. After two pre-periods, the initial state matches the final one. The quantities $\|\theta\|_2$ of PPO7 and PPO30 are almost indistinguishable as can be seen in figure 11 and as is usual for period-doubling bifurcations.

4.3. Symmetry subspace: four-fold translation

In this subsection, we discuss two time-periodic solutions (RPO12 and RPO20) identified in the symmetry subspace $\langle \tau(L_y/4, L_z/4) \rangle \sim Z_4$. Branches RPO12 and RPO20 are shown in the bifurcation diagram of figure 15.

4.3.1. RPO12: saddle-node and global bifurcations

RPO12 undergoes saddle-node bifurcations at $Ra = 6293.9$, $6643 \lesssim Ra \lesssim 6646$ and at $Ra = 6675.8$. The lower branch (in terms of period) of RPO12 has been continued until $(Ra, T) = (6680, 111.4)$ where we stopped the continuation. The upper branch is continued

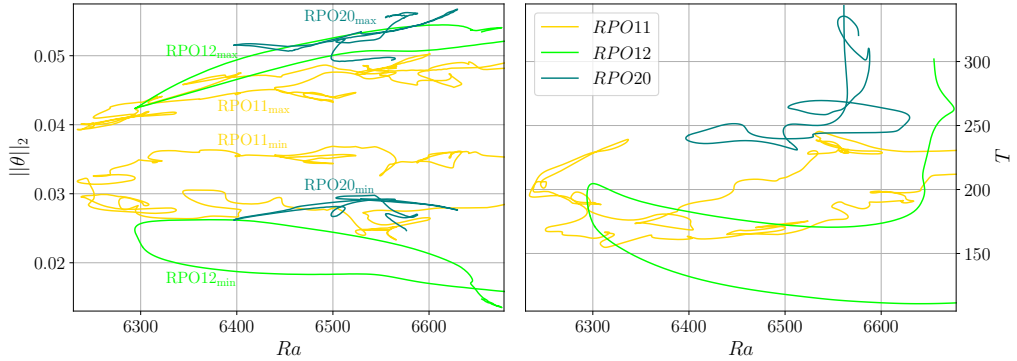


Figure 15: Temperature norms (left) and period (right) of RPO11, RPO12 and RPO20. Branch RPO11 undergoes saddle-node bifurcations and both the lower and upper branches are continued beyond $Ra = 6680$; its bifurcation structure remains unclear. The lower RPO12 branch exists beyond $Ra = 6680$, while the upper branch seems to terminate in a global bifurcation by meeting FP4, close to $Ra = 6655$. RPO20 bifurcates from FP4 in a global bifurcation at $Ra \approx 6561$ at which its period seems to diverge; its termination is unclear.

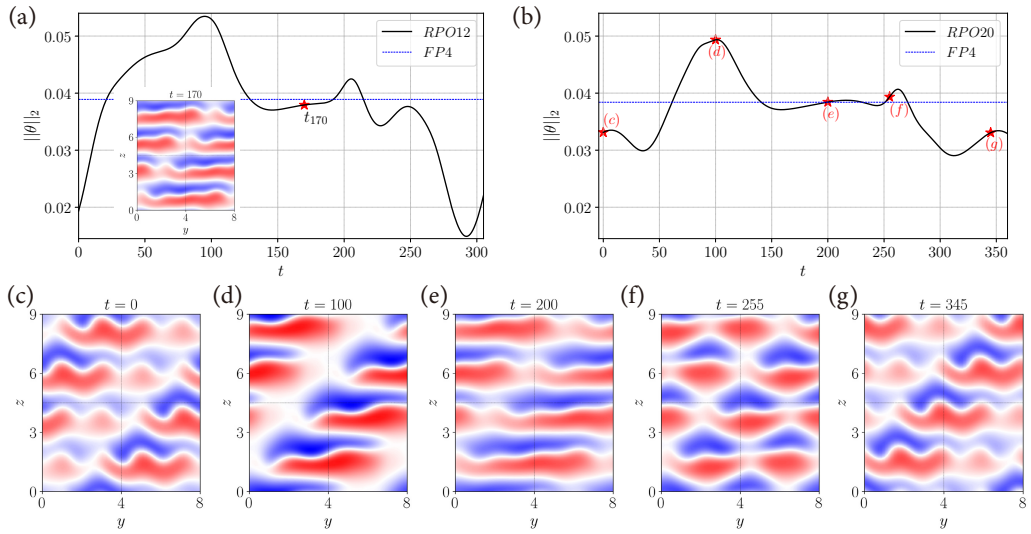


Figure 16: (a) Time series of RPO12 with relative period $T = 301.9$ at $Ra = 6654.865$. A snapshot of the midplane temperature field at instant $t = 170$ is shown in the inset and is close to FP4. (b) Time series of RPO20 with relative period $T = 343$ at $Ra = 6561.2$. The five red stars indicate the moments at which the snapshots (c)-(g) are taken. Snapshot (e) is close to FP4.

until $Ra = 6654.865$ where the relative period $T = 301.9$ is the highest that we were able to attain numerically.

Integrating RPO12 at $Ra = 6654.865$, we observe that the dynamics slows down slightly near a state that is close to FP4; see figure 16(a) and its inset. We subsequently used this state ($t = 170$) as the initial guess for Newton's method to converge to FP4 at $Ra = 6654.865$. Even though the plateau in figure 16(a) is not obvious and the period of RPO12 in figure 15 is not yet very long, our observations suggest that RPO12 terminates in a global homoclinic bifurcation by meeting FP4. This scenario is very similar to that of RPO20 to be discussed just after in §4.3.2, for which we will show more snapshots.

4.3.2. RPO20: saddle-node and global bifurcations

Although RPO20 exists in the range $6396.7 < Ra < 6629.6$, its two endpoints approach one another. We have continued RPO20 to $Ra = 6561.2$ with relative period $T = 343.6$ and to $Ra = 6576.46$ with $T = 320.45$. Close to $Ra = 6561.2$, its period seems to diverge, slightly more so than that of RPO12. Figure 16(b) shows the time series from a simulation of RPO20 at $Ra = 6561.2$, with the corresponding snapshots of the temperature field shown in figures 16(c-g). The plateau-like behaviour ($150 \lesssim t \lesssim 250$) in the time series as well as the close resemblance between figure 16(e) and FP4 suggest that RPO20 bifurcates from FP4 in a global homoclinic bifurcation at a nearby Rayleigh number.

By looking at the snapshots in figures 16(c-g), we notice that the dynamics is not very different from previous cases, as the reflection symmetry $\langle \pi_y \pi_{xz} \rangle$ is only weakly broken by the global bifurcation from FP4. Since it is clear that the RPO20 (and RPO12 in §4.3.1) with the longest period that we have succeeded in computing is still far from the actual homoclinic cycle, we do not discuss or show the eigendirections of FP4 along which RPO20 (and RPO12) may approach and escape from. The termination of the other end of the RPO20 branch is unclear and not discussed.

4.4. Symmetry subspace: two-fold translation

In this subsection, we discuss two relative periodic orbits (RPO5 and RPO8) identified in the symmetry subspace $\langle \tau(L_y/2, L_z/2) \rangle \sim Z_2$. Their branches are contained in the bifurcation diagram of figure 11, while their time series and snapshots are shown in figure 17.

4.4.1. RPO5: saddle-node and global bifurcations

In the Ra range we study, RPO5 undergoes a sequence of saddle-node bifurcations. The lower branch (in period) continues to exist until at least $Ra = 6635$. For the upper branch, the seemingly diverging period at $Ra \approx 6510.4$ suggests that RPO5 might disappear in a global bifurcation. We have been able to continue RPO5 until $Ra = 6510.4$ with relative period $T = 400.5$. Integrating RPO5 at $Ra = 6510.4$ in time, the dynamics slows down slightly close to FP4 ($t \approx 300$), as shown by the time series in figure 17(f) and the snapshot in figure 17(d). We expect that the time spent near FP4 would increase if we were able to continue RPO5 further.

4.4.2. RPO8: saddle-node bifurcations

As shown in figure 11, RPO8 undergoes a sequence of saddle-node bifurcations and is continued until $Ra = 6636.26$ (lower branch, where relative period $T = 246.97$) and $Ra = 6421.24$ (upper branch, where $T = 371.26$). With the available information, we have not been able to determine the origin of RPO8. Figures 17(h-l) show five snapshots of RPO8 at $Ra = 6388.46$. Like PPO7, rolls in RPO8 tend to distort and to develop defects, and the variation of $\|\theta\|_2$ along the orbit is large; compare for instance figures 17(h) and (j). Note also that figure 17(k) is similar to a less symmetric version of FP8 shown in figure 2(f).

4.5. Symmetry subspace: reflection with three-fold translation

Only one orbit is identified in the symmetry subspace $\langle \pi_y \pi_{xz}, \tau(L_y/3, L_z/3) \rangle \sim D_3$.

4.5.1. PO14: Hopf and global bifurcations

As shown in figure 8, PO14 bifurcates from FP11 at $Ra = 6289.6$ in a symmetry-preserving Hopf bifurcation. (For consistency with symmetry groups of other orbits, we do not introduce tilted coordinates for PO14 as we did for FP9-FP12 in §3.2. It can be verified that FP9, FP11 and FP12 all have the symmetry $\langle \pi_y \pi_{xz}, \tau(L_y/3, L_z/3) \rangle$ in the y - z coordinate.) The period

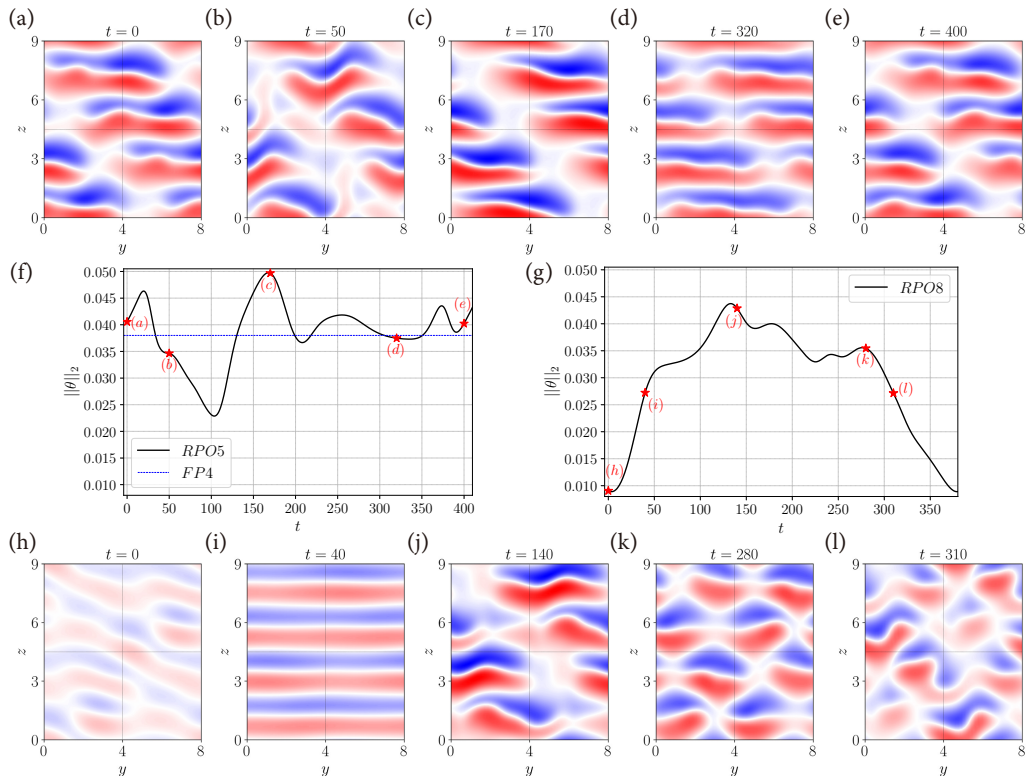


Figure 17: Dynamics of RPO5 with relative period $T = 400.5$ at $Ra = 6510.4$ and of RPO8 with $T = 375.4$ at $Ra = 6388.46$. (a-e, h-l) Snapshots of the midplane temperature field. Snapshot (d) of RPO5 is similar to FP4 (figure 2d) and converges to FP4 when used as an initial guess for Newton’s method. (f-g) Time series, initialized by the states shown in (a) and (h).

of PO14 close to the bifurcation point closely matches the value predicted by the bifurcating imaginary eigenvalue pair of FP11. FP9, FP10 and FP11 are called secondary, tertiary and quaternary states, respectively. PO14 can thus be called a quinary state. Forward continuation of PO14 suggests that it terminates in a global homoclinic bifurcation by meeting FP9, close to $Ra = 6313$ at which its period diverges.

Figures 18(a-d) show four snapshots of PO14 at $Ra = 6313$, the highest Rayleigh number that we have reached. The corresponding time series and phase space projection are shown in figures 18(e-f), with special instants indicated by red stars. The long plateau ($250 \lesssim t \lesssim 550$) in the time series and the clustering of points close to FP9 in the phase space projection suggest that PO14 approaches and slows down near FP9. Interestingly, the time series also shows another short plateau near $t \approx 690$, whose corresponding state, shown in figure 18(d), resembles FP12 shown in figure 2(j). However, the non-negligible difference of norms in both figures 18(e-f) between FP12 and the state shown in figure 18(d) suggests that PO14 does not visit FP12 closely. It might be possible that, if we were able to continue PO14 further with longer periods, FP12 would be visited more closely by PO14. But based on the available data, we conclude that PO14 ends by approaching a homoclinic cycle by meeting FP9.

In order to analyze this homoclinic cycle, we have computed the spectrum of FP9 at $Ra = 6313$. (Rather than referring back to figure 2(g), the reader can look at figure 18(c), which closely resembles FP9. For a detailed explanation of the correspon-

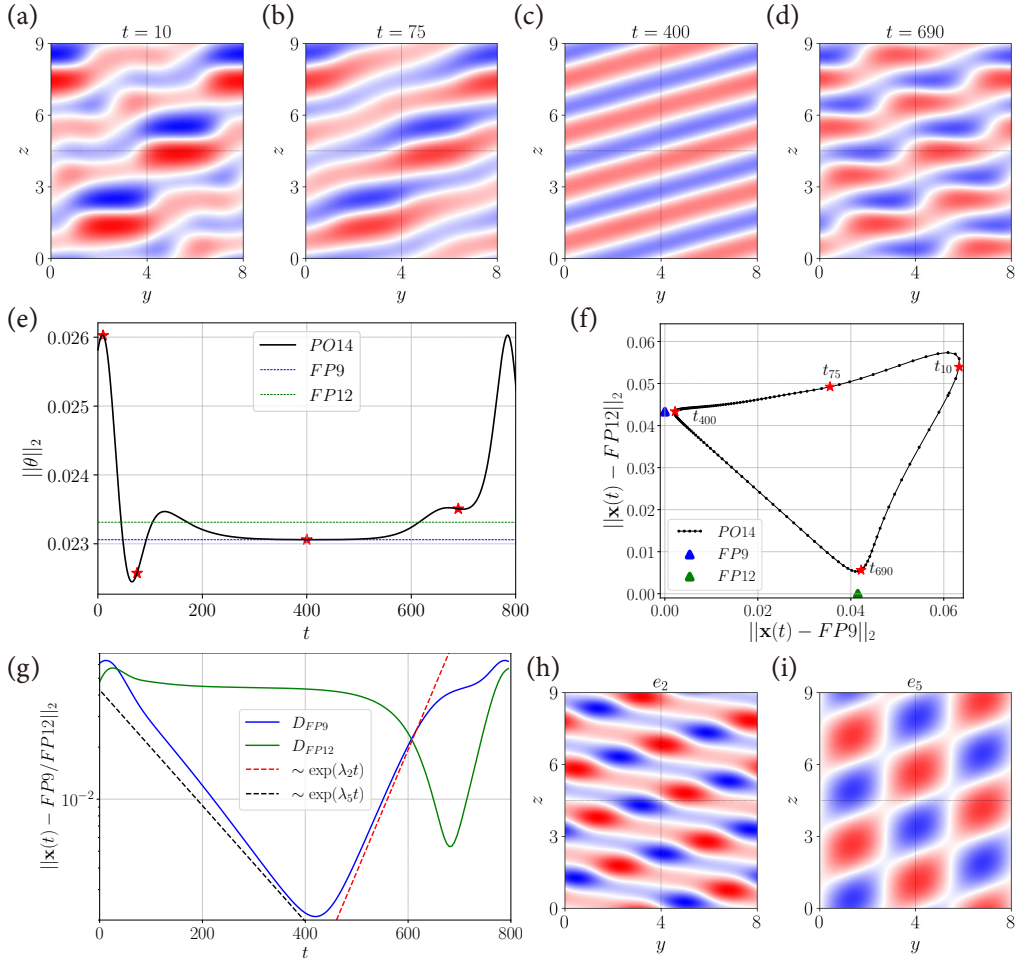


Figure 18: Dynamics of PO14 with period $T = 775.62$ at $Ra = 6313$ (close to the global bifurcation point). (a-d) Snapshots of the midplane temperature field. Snapshots (c) and (d) converge to FP9 and FP12 when used as initial guesses. (e) Time series from DNS. (f) Phase space projection: shown are PO14 (curve with dots) as well as FP9 and FP12 (triangles). In (e) and (f), the four red stars indicate the moments at which the snapshots (a)-(d) are taken. (g) L_2 -distance between each instantaneous flow field of PO14 and FP9 (and FP12). The dynamics of PO14 is exponential for most of the cycle (blue curve). The approaching (black dashed line) and escaping (red dashed line) dynamics of PO14 with respect to FP9 are shown and are governed by two eigenvalues, λ_2 and λ_5 , of FP9. (h-i) Two eigenmodes e_2 and e_5 of FP9, visualized via the midplane temperature field.

dence between global bifurcations and the eigenvalues of the fixed points that are approached by the trajectories, see [Zheng et al. \(2024c\)](#).) Restricting the computation to the symmetry subspace $\langle \pi_y, \pi_{xz}, \tau(L_y/3, L_z/3) \rangle$ gives seven leading eigenvalues, all real: $[\lambda_1, \lambda_2, \lambda_3, \lambda_4, \lambda_5, \lambda_6, \lambda_7] = [0.0256, 0.0162, 0.0105, 0.00075, -0.0077, -0.0087, -0.012]$. Since we imposed FP9's symmetries in the Arnoldi iterations, the two neutral eigenvalues corresponding to translations in the periodic directions y and z are not present. We have determined that the eigendirections along which PO14 leaves and approaches FP9 are e_2 and e_5 associated with λ_2 and λ_5 , respectively. These eigendirections are confirmed by subtracting FP9 from the instantaneous flow fields of PO14, and comparing the resulting

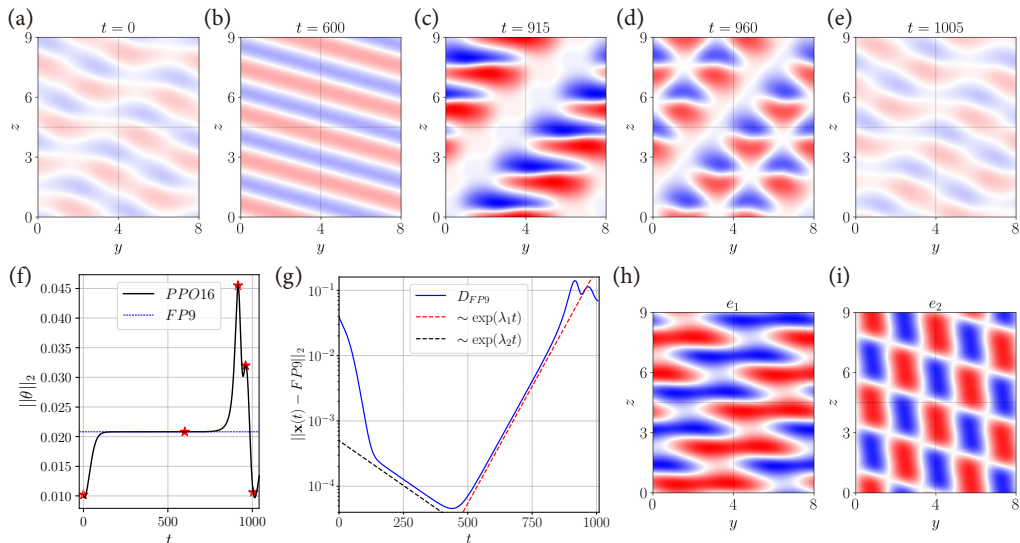


Figure 19: Dynamics of PPO16 with pre-period $T = 1007.05$ at $Ra = 6240.6429$ (close to the global bifurcation point). (a-e) Snapshots of the midplane temperature field. Snapshot (b) converges to FP9 when used as an initial guess. (f) Time series from DNS. The five red stars indicate the moments at which the snapshots (a)-(e) are taken. (g) L_2 -distance between each instantaneous flow field of PPO16 and FP9. The dynamics of PPO16 is exponential for most of the cycle (blue curve). The approaching (black dashed line) and escaping (red dashed line) dynamics of PPO16 with respect to FP9 are shown to be governed by two eigenvalues, λ_1 and λ_2 , of FP9. (h-i) Two eigenmodes e_1 and e_2 of FP9, visualized via the midplane temperature field.

fields with eigenmodes obtained by Arnoldi iterations, as well as by the close matches for the exponential growth and decay rate between PO14 and FP9, see figure 18(g).

The two relevant eigendirections can be interpreted and analyzed by comparing PO14 and FP9. Eigenmode e_2 , shown in figure 18(h), breaks the $O(2)$ symmetry of FP9 along its straight and homogeneous rolls by introducing alternating red and blue patches in this tilted direction; these patches lead to wavy-roll structures. It is not difficult to imagine that superposing FP9 (figure 18c) and e_2 gives approximately figure 18(d). Eigenmode e_5 , shown in figure 18(i), consists of a grid of red and blue rhombi, while figure 18(b) consists of rolls with bulges and constrictions. The colors of the rhombi are opposite to those of the bulges and the same as those of the constrictions. Thus, superposing e_5 on figure 18(b) reduces both distortions, restoring the broken symmetries of FP9.

4.6. Symmetry subspace: reflection with five-fold translation

Three orbits identified in the symmetry subspace $\langle \pi_y, \pi_{xz}, \tau(L_y/5, L_z/5) \rangle \sim D_5$ are discussed in this subsection. The dynamics of these three orbits appears to be similar and we only show snapshots of PPO16 (figures 19a-e) for illustration.

4.6.1. PPO16: global bifurcation

PPO16 is a pre-periodic orbit; its spatial phase shifts by $\langle \tau(L_y/10, L_z/10) \rangle$ after a pre-period; compare figures 19(a) and (e). After ten such pre-periods, the final state matches the initial state. The branch of PPO16 states is included in the bifurcation diagram of figure 8. We have continued PPO16 towards increasing Ra to $Ra = 6656.54$. Towards decreasing Ra , the period of PPO16 increases monotonically and eventually diverges, suggesting a global bifurcation. Figures 19(a-e) show five snapshots of PPO16 at $Ra = 6240.6429$ with pre-

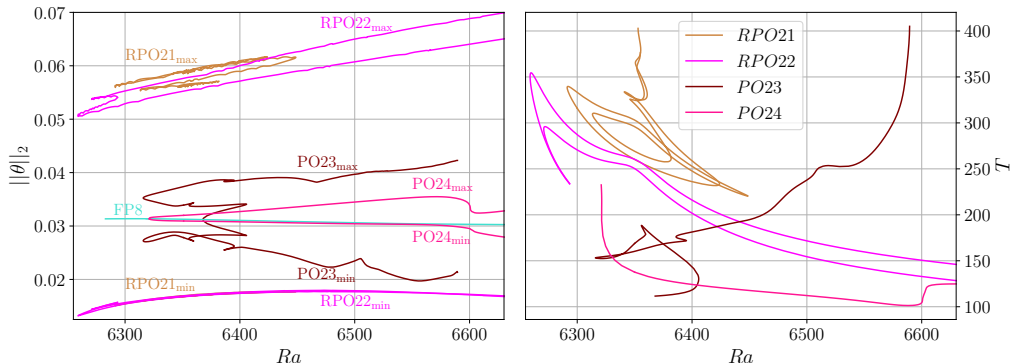


Figure 20: Temperature norms (left) and periods (right) of RPO21, RPO22, PO23 and PO24. On the left, the minima of $\|\theta\|_2$ of RPO21 and RPO22 are too close to be distinguished; the lack of smoothness in the maxima of $\|\theta\|_2$ of RPO21 corresponds to the overtaking of one temporal maximum or minimum of $\|\theta\|_2$ by another as Ra is varied. The creation and termination of RPO21 and RPO22 are not discussed. Both PO23 and PO24 bifurcate from FP8 in two Hopf bifurcations; PO23 possibly terminates in a global bifurcation at $Ra \approx 6589.5$ by meeting FP13, and PO24 exists until at least $Ra = 6667$.

period $T = 1007.05$, the lowest Rayleigh number we have reached. The corresponding time series in figure 19(f) indicates that PPO16 slows down significantly between $150 \lesssim t \lesssim 800$ and spends a long time near an oblique-roll state (figure 19b). This oblique-roll state is subsequently converged via Newton's method to FP9; figures 19(b) and 2(g) are related by π_y . Similarly to PO14 described in §4.5.1, PPO16 also bifurcates from FP9 in a global homoclinic bifurcation.

We computed the eigenvectors and eigenvalues of FP9 at $Ra = 6240.6429$ in the symmetry subspace $\langle \pi_y \pi_{xz}, \tau(L_y/5, L_z/5) \rangle$. The Arnoldi iterations return five leading eigenvalues, all real: $[\lambda_1, \lambda_2, \lambda_3, \lambda_4, \lambda_5] = [0.01651, -0.00631, -0.057, -0.0628, -0.07664]$. Clearly, PPO16 escapes from FP9 along e_1 , associated with λ_1 and shown in figure 19(h), the only unstable eigendirection in this subspace. The direction along which PPO16 approaches FP9 is e_2 , associated with the second eigenvalue λ_2 and shown in figure 19(i). These two eigendirections are subsequently confirmed by subtracting FP9 from PPO16, as well as by the exponential decay and growth rates shown in figure 19(g). Similarly to the scenario for PO14, here e_1 breaks the $O(2)$ symmetry of FP9 in the tilted direction and e_2 restores them.

4.6.2. RPO21 and RPO22: saddle-node bifurcations

Two relative periodic orbits RPO21 and RPO22 are shown in the bifurcation diagram of figure 20; both undergo a sequence of saddle-node bifurcations, and the termination and/or creation of both orbits remain unclear. RPO21 exists over the short range $6291.23 < Ra < 6448.75$; its two endpoints are quite close together, at $(Ra, T) = (6352.99, 402.83)$ and $(Ra, T) = (6354.95, 376.35)$. Integrating RPO21 in time at these two values of Ra does not show remarkable behavior or a close approach to a fixed point that would indicate a global bifurcation. RPO22 originates in a saddle-node bifurcation at $Ra = 6259$; the two branches which emanate from it can be continued at least until $Ra = 6667$.

4.7. Symmetry subspace: reflection

In this subsection, we discuss two periodic orbits, PO23 and PO24 that are in the symmetry subspace $\langle \pi_y \pi_{xz} \rangle \sim Z_2$. As shown in figure 20, both bifurcate from FP8 at $Ra = 6367.9$ and $Ra = 6321$, in two Hopf bifurcations which preserve the reflection symmetry of FP8, and break its translation symmetry $\langle \tau(L_y/2, 0) \rangle$.

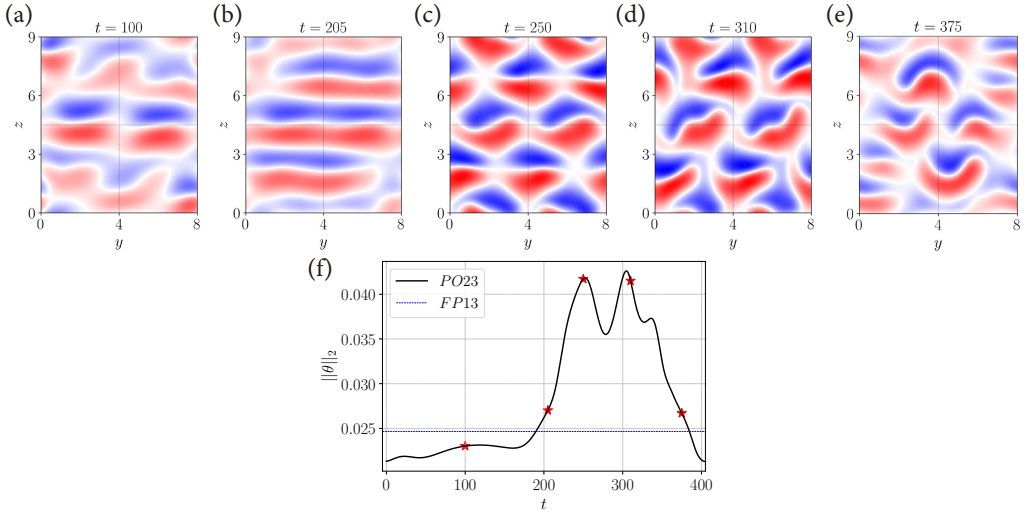


Figure 21: Dynamics of PO23 at $Ra = 6589.47$ with period $T = 404.6$. (a-e) Snapshots of the midplane temperature field. (f) Time series from DNS. The five red stars indicate the moments at which the snapshots (a)-(e) are taken.

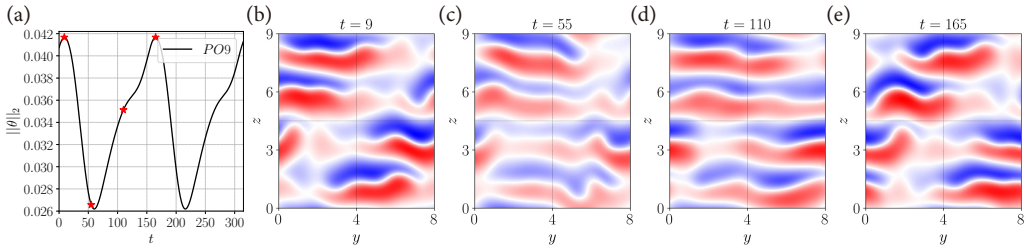


Figure 22: Dynamics of PO9 with period $T = 311.18$ at $Ra = 6413.11$. (a) Time series from DNS. The four red stars indicate the moments at which the snapshots (b)-(e) are taken.

4.7.1. PO23: Hopf, saddle-node and global bifurcations

After its creation, PO23 undergoes a sequence of saddle-node bifurcations. Figures 21(a-e) show five snapshots of PO23 at $Ra = 6589.47$. The initial phase ($25 \leq t \leq 175$) of PO23 resembles FP13; compare figure 21(a) and figure 2(k). We have been able to continue PO23 until $Ra = 6589.47$, where its period is $T = 404.6$. Figure 20 shows that its period seems to diverge; we believe that PO23 terminates on FP13 in a global bifurcation point.

4.7.2. PO24: Hopf bifurcation

After bifurcating from FP8 at $Ra = 6321$, PO24 is continued until $Ra = 6667$ where we stopped the continuation. It is clear that PO24 oscillates around FP8 and the oscillation amplitude is smaller than that of PO23. We do not show snapshots of PO24.

4.8. No spatial symmetry

In this subsection, we discuss two orbits without any spatial symmetries.

4.8.1. PO9: saddle-node bifurcations

PO9 is shown in the bifurcation diagram of figure 11. PO9 undergoes a sequence of saddle-node bifurcations. We have continued the lower branch (in period) of PO9 until $(Ra, T) =$

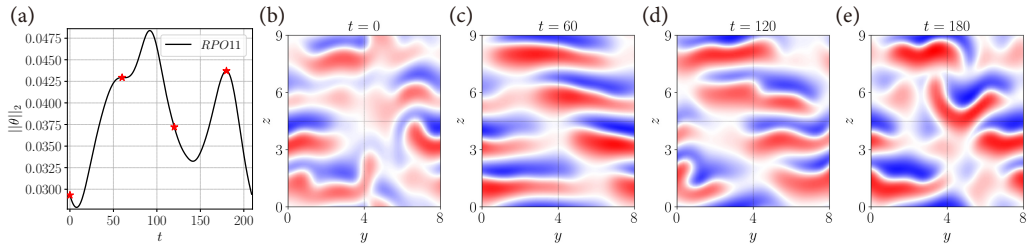


Figure 23: Dynamics of RPO11 with relative period $T = 209.26$ at $Ra = 6500$. (a) Time series from DNS. The four red stars indicate the moments at which the snapshots (b)-(e) are taken.

(6631.4, 188.7) and the upper branch until $(Ra, T) = (6436.72, 323.05)$; the origin of PO9 remains unclear. Snapshots and time series of PO9 at $Ra = 6413.11$ are shown in figure 22. Comparing snapshots (b) and (e), we notice that PO9 has the spatio-temporal symmetry

$$(u, v, w, \theta)(x, y, z, t + T/2) = \pi_y \pi_{xz} (u, v, w, \theta)(x, y + 0.11L_y, z + 0.03L_z, t), \quad (4.5)$$

where T is the period of PO9. Since (4.5) contains the combined reflection operator $\pi_y \pi_{xz}$, after two such pre-periods, the discrete translations in L_y and L_z cancel out and the final state is identical to the initial state—an actual periodic orbit which we converged in our study.

4.8.2. RPO11: saddle-node bifurcations

Branch RPO11 is contained in the bifurcation diagram of figure 15. RPO11 undergoes a sequence of saddle-node bifurcations. We stopped the continuation at $(Ra, T) = (6680, 212)$ for the lower branch and at $(Ra, T) = (6680, 230.6)$ for the upper branch; its origin remains unknown. Figures 23(b-e) show four snapshots of RPO11 at $(Ra, T) = (6500, 209.26)$. Like several of the other periodic orbits, RPO11 contains a state (figure 23c) with four relatively straight but deformed rolls, which breaks along a diagonal fault line (figure 23d), leading to disordered states (figure 23e,b), which then reform into approximate rolls (figure 23c).

5. Discussion, conclusions and outlook

In this work, we discussed 26 newly identified periodic orbits in the vertical thermal convection system at fixed Prandtl number $Pr = 0.71$ in a fixed-size domain $[L_x, L_y, L_z] = [1, 8, 9]$ and in the Rayleigh number range $6225 \lesssim Ra \lesssim 6650$. These orbits are classified in terms of their spatial symmetries, and eight different symmetry groups are identified. The bifurcations that these time-periodic solutions undergo are summarized in table 1.

As noticed throughout §4 and in table 1, almost all of the periodic orbits we discuss undergo multiple saddle-node bifurcations. Because of this, there exist several periodic orbits at the same Rayleigh number with different periods, on different portions of the same solution branch. As saddle-node bifurcations do not break the spatial symmetries of a state, these orbits all have the same symmetry but different dynamics and thus different statistics. Zheng *et al.* (2024a) report the ghost states resulting (“bifurcating”) from a saddle-node bifurcation, which resemble the converged solutions at the saddle-node bifurcation. Such ghosts influence locally the trajectory of the chaotic dynamics near a saddle-node bifurcation and are relevant for the spatio-temporal patterns observed in weakly turbulent flows.

Local (Hopf) and global (heteroclinic or homoclinic) bifurcations are two standard scenarios by which periodic orbits are created or destroyed. We have found three orbits which are born from equilibria in Hopf bifurcations, and eight orbits that disappear or appear via global bifurcations. The formation of a periodic orbit from a fixed point via a Hopf bifurcation corresponds to the change of sign of the real part of a complex conjugate

Spatial symmetry	Periodic orbit	Bifurcations	Discussed in	Shown in figure(s)
$\langle \pi_y \pi_{xz}, \tau(L_y/4, L_z/4) \rangle$	PO1	H, SN, GB	Zheng <i>et al.</i> (2024c)	5, 6, 7, 8, 15
$\langle \pi_y \pi_{xz}, \tau(L_y/4, L_z/4) \rangle$	PO2	PD, SN, GB	Zheng <i>et al.</i> (2024c)	5, 9, 10, 11, 15
$\langle \tau(L_y/2, L_z/2) \rangle$	PO3	PF	Zheng <i>et al.</i> (2024c)	5, 13, 15
$\langle \pi_y, \pi_{xz} \tau(L_y/2, 0) \rangle$	PO4	H	Zheng <i>et al.</i> (2024c)	5, 14, 15
$\langle \pi_y \pi_{xz}, \tau(L_y/4, L_z/4) \rangle$	RPO13	PD	§4.1.1	4
$\langle \pi_y \pi_{xz}, \tau(L_y/4, L_z/4) \rangle$	RPO15	SN, isola	§4.1.2	4
$\langle \pi_y \pi_{xz}, \tau(L_y/4, L_z/4) \rangle$	RPO17	SN, isola	§4.1.2	5
$\langle \pi_y \pi_{xz}, \tau(L_y/4, L_z/4) \rangle$	RPO26	SN, isola	§4.1.2	4
$\langle \pi_y \pi_{xz}, \tau(L_y/4, L_z/4) \rangle$	RPO28	SN, isola	§4.1.2	4
$\langle \pi_y \pi_{xz}, \tau(L_y/4, L_z/4) \rangle$	RPO18	SN, GB	§4.1.3	5, 6
$\langle \pi_y \pi_{xz}, \tau(L_y/4, L_z/4) \rangle$	RPO19	PD, SN	§4.1.4	7
$\langle \pi_y \pi_{xz}, \tau(L_y/2, L_z/2) \rangle$	PO6	SN, GB	§4.2.1	8, 9, 10
$\langle \pi_y \pi_{xz}, \tau(L_y/2, L_z/2) \rangle$	PPO7	SN, isola	§4.2.2	11, 12
$\langle \pi_y \pi_{xz}, \tau(L_y/2, L_z/2) \rangle$	RPO10	SN, GB	§4.2.3	8, 13
$\langle \pi_y \pi_{xz}, \tau(L_y/2, L_z/2) \rangle$	RPO25	PF, SN, PH	§4.2.4	7
$\langle \pi_y \pi_{xz}, \tau(L_y/2, L_z/2) \rangle$	RPO27	PF, SN	§4.2.5	5
$\langle \pi_y \pi_{xz}, \tau(L_y/2, L_z/2) \rangle$	RPO29	SN, GB	§4.2.6	8, 14
$\langle \pi_y \pi_{xz}, \tau(L_y/2, L_z/2) \rangle$	PPO30	PD	§4.2.7	11
$\langle \tau(L_y/4, L_z/4) \rangle$	RPO12	SN, GB	§4.3.1	15, 16
$\langle \tau(L_y/4, L_z/4) \rangle$	RPO20	SN, GB	§4.3.2	15, 16
$\langle \tau(L_y/2, L_z/2) \rangle$	RPO5	SN, GB	§4.4.1	11, 17
$\langle \tau(L_y/2, L_z/2) \rangle$	RPO8	SN	§4.4.2	11, 17
$\langle \pi_y \pi_{xz}, \tau(L_y/3, L_z/3) \rangle$	PO14	H, GB	§4.5.1	8, 18
$\langle \pi_y \pi_{xz}, \tau(L_y/5, L_z/5) \rangle$	PPO16	GB	§4.6.1	8, 19
$\langle \pi_y \pi_{xz}, \tau(L_y/5, L_z/5) \rangle$	RPO21	SN	§4.6.2	20
$\langle \pi_y \pi_{xz}, \tau(L_y/5, L_z/5) \rangle$	RPO22	SN	§4.6.2	20
$\langle \pi_y \pi_{xz} \rangle$	PO23	H, SN, GB	§4.7.1	20, 21
$\langle \pi_y \pi_{xz} \rangle$	PO24	H	§4.7.2	20
No spatial symmetry	PO9	SN	§4.8.1	11, 22
No spatial symmetry	RPO11	SN	§4.8.2	15, 23

Table 1: Summary of spatial symmetries and bifurcation scenarios of 30 periodic orbits found in domain $[L_x, L_y, L_z] = [1, 8, 9]$, with PO1-PO4 discussed in Zheng *et al.* (2024c). PF, SN, PD, PH, H and GB are abbreviations for pitchfork, saddle-node, period-doubling, period-halving, Hopf and global bifurcations.

eigenvalue pair of the fixed point. In contrast, the formation of a heteroclinic or homoclinic cycle via a global bifurcation does not correspond to the passage of an eigenvalue and hence cannot be detected by linear stability analysis; instead, it corresponds to the formation of a trajectory joining two saddles or joining one saddle to itself. The period diverges at such bifurcation points, which makes them challenging to compute, but we have been able to continue heteroclinic and homoclinic cycles here, as we did in Zheng *et al.* (2024c).

Five isolas are found. Even though they are isolas in our bifurcation diagrams, i.e. in parameter regime that we investigate, they might undergo other types of bifurcations if other parameters were varied (e.g. inclination angle, Prandtl number or domain size); we do not explore this. Several orbits (RPO8, PO9, RPO11, RPO21 and RPO22) are of unknown bifurcation-theoretic origins in the Rayleigh number range we study.

Finally, we comment on the computational cost and time consumed during this project. We used approximately ten million CPU hours within eight months to converge these orbits

via Newton’s method and to continue them in Rayleigh number. There certainly exist many more solution branches to be found; those bifurcating from the known branches via local bifurcations or global bifurcations, as well as unconnected branches. One might question the utility of computing many of these time-periodic states, except to explore and understand the very complicated bifurcation structures of the Navier-Stokes and Boussinesq equations. This valid concern will be discussed in detail in our upcoming manuscript showing the reconstruction of the statistics of a transitional turbulent flow based on the periodic orbits we find (Cvitanović & Eckhardt 1991).

Acknowledgements. We thank O. Ashtari for helpful discussions. We are grateful to the Scientific IT and Application Support (SCITAS) team of EPFL for providing computational resources and high performance computing (HPC) expertise.

Funding. This work was supported by the European Research Council (ERC) under the European Union’s Horizon 2020 research and innovation programme (grant no. 865677).

Declaration of interests. The authors report no conflict of interest.

Author ORCIDs.

Zheng Zheng <https://orcid.org/0000-0002-9833-1347>;

Laurette S. Tuckerman <https://orcid.org/0000-0001-5893-9238>;

Tobias M. Schneider <https://orcid.org/0000-0002-8617-8998>.

Appendix A. Grid resolution verification

In order to verify that our results are independent of the grid resolution, we have reconverged RPO15 and RPO18—both showing slight lack of smoothness in the curves of bifurcation diagram—by employing the new refined grid ($[N_x, N_y, N_z] = [41, 136, 136]$) and reconstructed their bifurcation diagrams. The differences in L_2 -norm of temperature field $\|\theta\|_2$, periods and locations (in terms of Ra) of saddle-node bifurcations between original and new grids are all below 10^{-4} . We believe that these numbers are acceptable for a change of grid and we do not expect these to be of the order of machine precision as the criterion used for converging invariant solutions.

REFERENCES

- ARMBRUSTER, DIETER, GUCKENHEIMER, JOHN & HOLMES, PHILIP 1988 Heteroclinic cycles and modulated travelling waves in systems with $O(2)$ symmetry. *Physica D* **29** (3), 257–282.
- CHANDLER, GARY J & KERSWELL, RICH R 2013 Invariant recurrent solutions embedded in a turbulent two-dimensional Kolmogorov flow. *J. Fluid Mech.* **722**, 554–595.
- CVITANOVIĆ, PREDRAG 1991 Periodic orbits as the skeleton of classical and quantum chaos. *Physica D* **51**, 138–151.
- CVITANOVIĆ, PREDRAG 2013 Recurrent flows : the clockwork behind turbulence. *J. Fluid Mech.* **726**, 1–4.
- CVITANOVIĆ, PREDRAG & ECKHARDT, BRUNO 1991 Periodic orbit expansions for classical smooth flows. *J. Phys. A: Math. Gen.* **24**, L237–L241.
- DANIELS, KAREN, PLAPP, BRENDAN & BODENSCHATZ, EBERHARD 2000 Pattern Formation in Inclined Layer Convection. *Phys. Rev. Lett.* **84**, 5320–5323.
- GAO, ZHENLAN, PODVIN, BERENGERE, SERGENT, ANNE, XIN, SHIHE & CHERGUI, JALEL 2018 Three-dimensional instabilities of natural convection between two differentially heated vertical plates: Linear and nonlinear complementary approaches. *Phys. Rev. E* **97**, 053107.
- GIBSON, JOHN F, REETZ, FLORIAN, AZIMI, SAJJAD, FERRARO, ALESSIA, KREILOS, TOBIAS, SCHROBSORFF, HECKE, FARANO, MIRKO, YESIL, AYSE FERHAN, SCHÜTZ, SIMON S, CULPO, MASSIMILIANO & SCHNEIDER, TOBIAS M 2019 Channelflow 2.0. Available at: <https://www.channelflow.ch>.
- GRAHAM, MICHAEL D. & FLORYAN, DANIEL 2021 Exact Coherent States and the Nonlinear Dynamics of Wall-Bounded Turbulent Flows. *Annu. Rev. Fluid Mech.* **53**, 227–253.

- KAWAHARA, GENTA & KIDA, SHIGEO 2001 Periodic motion embedded in plane Couette turbulence: Regeneration cycle and burst. *J. Fluid Mech.* **449**, 291–300.
- KAWAHARA, GENTA, UHLMANN, MARKUS & VAN VEEN, LENNAERT 2012 The Significance of Simple Invariant Solutions in Turbulent Flows. *Annu. Rev. Fluid Mech.* **44**, 203–225.
- KRUPA, MARTIN 1997 Robust heteroclinic cycles. *J. Nonlinear Sci.* **7** (2), 129–176.
- LUCAS, DAN & KERSWELL, RICH R. 2015 Recurrent flow analysis in spatiotemporally chaotic 2-dimensional Kolmogorov flow. *Physics of Fluids* **27** (4).
- NAGATA, M 1990 Three-dimensional finite-amplitude solutions in plane Couette flow: bifurcation from infinity. *J. Fluid Mech.* **217**, 519–527.
- BOROŃSKA, KATARZYNA & TUCKERMAN, LAURETTE S. 2010a Extreme multiplicity in cylindrical rayleigh-bénard convection. i. time dependence and oscillations. *Phys. Rev. E* **81**, 036320.
- BOROŃSKA, KATARZYNA & TUCKERMAN, LAURETTE S. 2010b Extreme multiplicity in cylindrical rayleigh-bénard convection. ii. bifurcation diagram and symmetry classification. *Phys. Rev. E* **81**, 036321.
- PAGE, JACOB, NORGAARD, PETER, BRENNER, MICHAEL P. & KERSWELL, RICH R. 2024 Recurrent flow patterns as a basis for two-dimensional turbulence: Predicting statistics from structures. *Proc. Natl. Acad. Sci. U.S.A.* **121** (23), 1–10.
- REETZ, FLORIAN, KREILOS, TOBIAS & SCHNEIDER, TOBIAS M. 2019 Exact invariant solution reveals the origin of self-organized oblique turbulent-laminar stripes. *Nature Communications* **10** (1), 1–6.
- REETZ, FLORIAN & SCHNEIDER, TOBIAS M. 2020a Invariant states in inclined layer convection. Part 1. Temporal transitions along dynamical connections between invariant states. *J. Fluid Mech.* **898**, A22.
- REETZ, FLORIAN, SUBRAMANIAN, PRIYA & SCHNEIDER, TOBIAS M. 2020b Invariant states in inclined layer convection. Part 2. Bifurcations and connections between branches of invariant states. *J. Fluid Mech.* **898**, A23.
- ZHENG, ZHENG, BECK, PIERRE, YANG, TIAN, ASHTARI, OMID, PARKER, JEREMY P & SCHNEIDER, TOBIAS M 2024a Ghost states underlying spatial and temporal patterns: how non-existing invariant solutions control nonlinear dynamics, arXiv: 2411.10320.
- ZHENG, ZHENG, TUCKERMAN, LAURETTE S. & SCHNEIDER, TOBIAS M. 2024b Natural convection in a vertical channel. Part 1. Wavenumber interaction and Eckhaus instability in a narrow domain. *J. Fluid Mech.* **1000**, A28.
- ZHENG, ZHENG, TUCKERMAN, LAURETTE S. & SCHNEIDER, TOBIAS M. 2024c Natural convection in a vertical channel. Part 2. Oblique solutions and global bifurcations in a spanwise-extended domain. *J. Fluid Mech.* **1000**, A29.